

Variations in the P-T-t of Deformation in a Crustal-Scale Shear Zone in Metagranite

T. K. Cawood¹, and J. P. Platt¹

¹ Department of Earth Science, University of Southern California, Los Angeles, CA, USA

Corresponding author: T. K. Cawood (cawood.tk@gmail.com)

Key Points:

- The conditions of deformation in crustal-scale shear zones may vary spatially (with depth) and temporally (due to dip-slip motion).
- We use a multidisciplinary approach to quantify the timing and pressure-temperature conditions of shearing in the Simpon Shear Zone.
- Exposed rocks preserve evidence of deformation conditions from ~490°C and 6.7 kbar at ~24.5 Ma, to ~304°C and 1.5 kbar at 11.3 Ma.

Abstract

Deformation in crustal-scale shear zones occurs over a range of pressure-temperature-time (P-T-t) conditions, both because they may be vertically extensive structures that simultaneously affect material from the lower crust to the surface, and because the conditions at which any specific volume of rock is deformed evolve over time, as that material is advected by fault activity. Extracting such P-T-t records is challenging, because structures may be overprinted by progressive deformation. In addition, granitic rocks in particular may lack synkinematic mineral assemblages amenable to traditional metamorphic petrology and petrochronology. We overcome these challenges by studying the normal-sense Simplon Shear Zone in the central Alps, where strain localization in the exhuming footwall caused progressive narrowing of the shear zone, resulting in a zonation from high-T shearing preserved far into the footwall, to low-T shearing adjacent to the hangingwall. The Ti-in-quartz and Si-in-phengite thermobarometers yield deformation P-T conditions, as both were reset synkinematically, and although the sheared metagranites lack typical petrochronometers, we estimate the timing of deformation by comparing our calculated deformation temperatures to published thermochronological ages. The exposed SSZ footwall preserves evidence for retrograde deformation during exhumation, from just below amphibolite-facies conditions (490.2°C, 6.73 kbar) at ~24.5 Ma, to lower greenschist-facies conditions (303.7°C, 1.51 kbar) at ~11.3 Ma, with subsequent slip taken up by brittle faulting. Comparison to independent constraints on the maximum and minimum P-T-t conditions, and to alternate approaches for estimating P-T, suggests that our results may be reasonable, or may underestimate temperatures by up to ~30-90°C.

Plain Language Summary

Major shear zones deform material over a wide range of conditions, from low pressures and temperatures near the Earth's surface, where rocks are brittle, to high pressures and temperatures in the deep crust, where they are ductile and flow like warm toffee. The age and conditions of deformation can be estimated using mineral chemistry. However, this is difficult where rocks have been deformed over a range of conditions at different times. It is especially challenging in granite, which commonly lacks traditionally used minerals. In studying the Simplon Shear Zone, we overcome these challenges by carefully investigating its structure to untangle the deformation stages; by using the chemistry of quartz and phengite to estimate deformation conditions, both of which occur in granite; and by linking our temperatures to a published cooling history, to determine when our samples were deformed. We show that exposed rocks deformed between ~490°C at 6.7 kbar (~25 km depth) approximately 24.5 million years ago, and ~300°C at 1.5 kbar (~6 km) approximately 11 million years ago. Subsequent deformation was taken up by brittle faulting. Comparison to independent constraints and alternative approaches suggest that our results may be correct, or may underestimate conditions by up to ~30-90°C.

1 Introduction

The crustal-to lithospheric-scale shear zones that accommodate relative plate motions play a major role in generating seismic hazard, influencing the evolution of orogens, and controlling the distribution of ore deposits, and are fundamental in enabling plate tectonics (Cox et al., 2006; Handy et al., 2007). Understanding the time period and conditions over which such structures are active is thus vital for quantifying the rheology of the lithosphere, modelling deformation, reconstructing the tectonic evolution of regions, and determining the economic prospectivity of areas (Huntington & Klepeis, 2018; Oriolo et al., 2018). However, estimating

the pressure-temperature-time (P-T-t) conditions of deformation in large-scale shear zones remains challenging for several reasons: a) Deformation occurs over a range of different P-T conditions, which vary both spatially (with depth) and temporally (as material is advected, either by the fault zone itself or by movement on other structures); b) many mineral thermobarometers and chronometers reflect the conditions and timing of metamorphic mineral growth or magma emplacement, rather than deformation (Anderson, 1996; Anderson et al., 2008; Steffen & Selverstone, 2006); c) mineral thermochronometers yield insight into when their host rock cooled through a specific temperature (Reiners et al., 2018; Stockli, 2005), but these “cooling ages” do not necessarily reflect when that specific volume of rock was undergoing deformation (Oriolo et al., 2018); and d) much of the continental crust comprises rocks with a granitic to tonalitic composition (Rudnick & Gao, 2004; Wedepohl, 1995), and fewer thermobarometers are available in these high-variance compositions than for rocks with a low-variance pelitic or basaltic composition (Anderson, 1996; Anderson et al., 2008; Caddick & Thompson, 2008; Massonne, 2015; White et al., 2014).

The aim of this study is therefore to investigate how the P-T-t conditions of deformation vary within Simplon Shear Zone (SSZ) in the Central Alps, a normal-sense shear zone developed predominantly in metagranite. It is well documented that the exposed footwall underwent deformation at a range of P-T conditions during exhumation and cooling (Campani et al., 2010a; Haertel et al., 2013; Mancktelow, 1985), and the P-T-t conditions of peak metamorphism are constrained (Baxter & DePaolo, 2000; Vance & O’Nions, 1992). In addition, there is a significant body of thermochronological data bracketing the time window of deformation (Campani et al., 2010b; Grasemann & Mancktelow, 1993), but scarce absolute, unambiguous ages of syn-kinematic petrochronological phases that can be linked to deformation at specific conditions.

We overcome the challenges outlined above by combining careful microscopy with mineral chemistry, whole-rock geochemical modeling, and thermochronological data, and test this approach by comparing our results to independently-derived P-T-t constraints. Whole-rock compositions are used to model the expected Si content of phengite and Ti content of quartz over a range of conditions, because both vary as a function of pressure and temperature (Massonne & Schreyer, 1987; Thomas et al., 2010; Wark & Watson, 2006). These models are compared to the measured Si in phengite and Ti in quartz that, based on their microstructure, chemistry, and textural relations, appear to have been re-equilibrated together during deformation. This approach has recently been used to estimate deformation conditions in metapsammites from the Moine Thrust in Scotland (Lusk & Platt, in press). It benefits from using minerals typically present in rocks of granitic or similar compositions, and which are commonly involved in deformation over a wide P-T range and thus have the potential to re-equilibrate to reflect deformation conditions (Ashley et al., 2014; Bestmann & Pennacchioni, 2015; Grujic et al., 2011; Nachlas et al., 2018; Santamariá-López et al., 2019). In addition, incorporating the bulk rock chemistry allows us to model the TiO_2 activity (a_{TiO_2}), a key constraint required to use Ti-in-quartz thermometry (Ashley & Law, 2015; Thomas et al., 2010), as well as the Si content of phengite, which in addition to pressure and temperature, is sensitive to bulk composition (Massonne & Schreyer, 1987; Massonne & Szpurka, 1997). By comparing our calculated deformation temperatures to thermochronometers with similar cooling temperatures, at comparable positions within the SSZ footwall, we also link each sample to an age of deformation.

2 Geological Setting

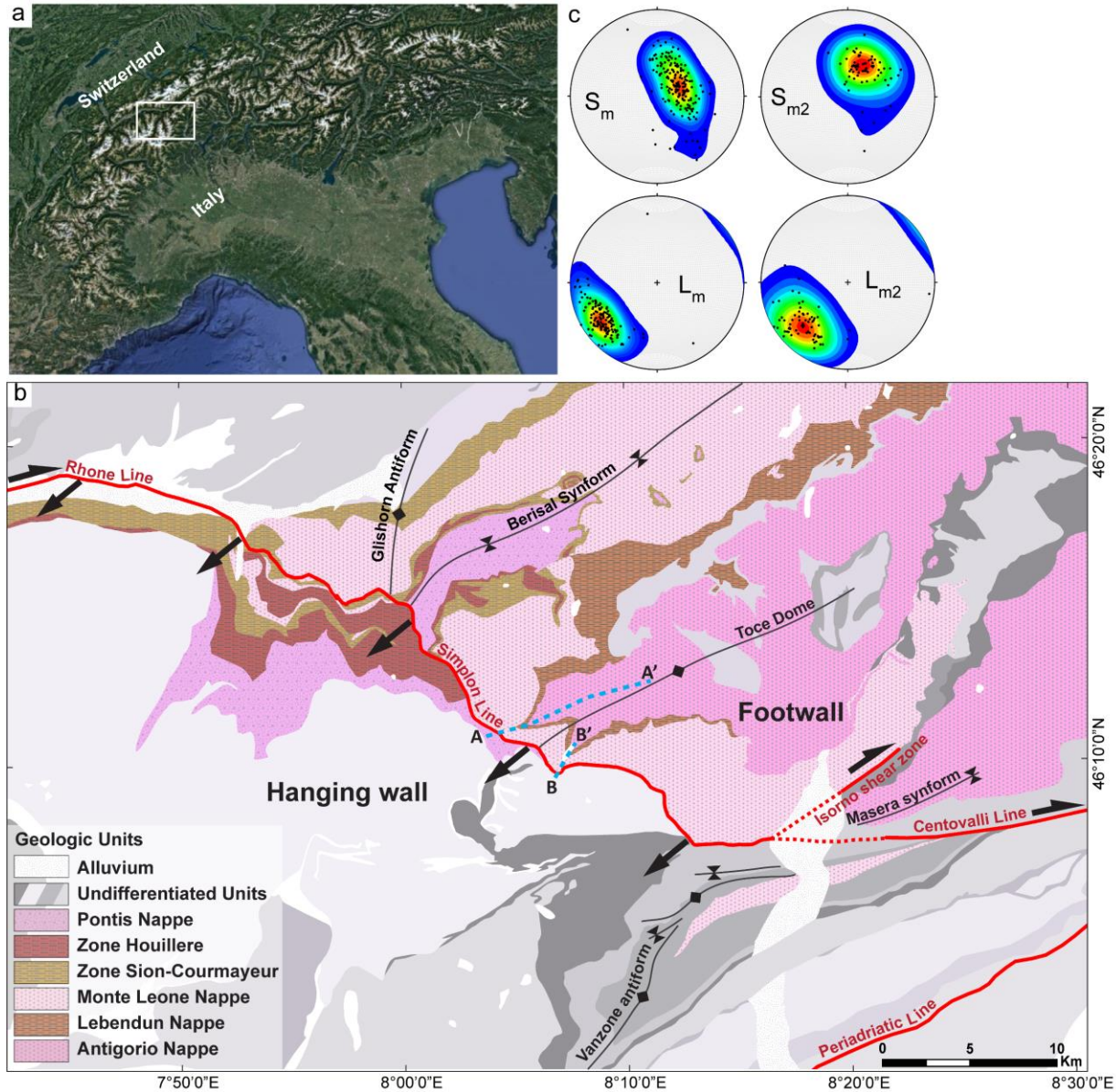
2.1 The Simplon Shear Zone

The Simplon Fault Zone is a crustal-scale, low-angle, ductile-to-brittle, normal-sense structure in the Central Alps (Fig. 1), which accommodated orogen-parallel extension during collision between the European plate and the Adriatic indenter (Campani et al., 2010a; Mancktelow, 1985; Steck, 2008). It separates Upper Penninic nappes in the downthrown hangingwall, derived from the Briançonnais microcontinent and the Neo-Tethys ocean basin, from lower Penninic nappes in the exhumed footwall, derived from the basement of the European passive margin (Mancktelow, 1985; Steck, 2008). This exhumed footwall forms the Toce Dome, the western portion of the regional Lepontine Gneiss Dome. Oligocene updoming was contemporaneous with peak Barrovian metamorphic conditions and distributed E-W-directed ductile extension, the later stages of which were synchronous with motion on the retrograde Simplon Fault Zone (Steck, 2008; Steck & Hunziker, 1994; Vance & O’Nions, 1992).

The Simplon Fault Zone comprises a broad zone of ductile mylonites extending several kilometers into the footwall (the Simplon Shear Zone, SSZ), which transition structurally upwards into the brittle Simplon Line, a narrow cataclastic zone overprinting the ductile deformation (Mancel & Merle, 1987; Mancktelow, 1985). Across the SSZ, metamorphic isograds are offset, and a distinct jump in thermochronological ages is observed (Campani et al., 2010a). In the central part of the SSZ, mylonites dip ca. 25-30° to the SW, and are associated with a variety of top-down-to-SW shear-sense indicators, including quartz CPOs, feldspar sigma clasts, oblique quartz grain shape fabrics, and shear bands (Mancktelow, 1985, 1987).

The SSZ is well studied, with over 170 years of publications (e.g. Gerlach, 1869; Schardt, 1903; Studer, 1851, to Bergemann et al., 2020). A significant body of knowledge is thus available for the SSZ, including detailed structural mapping highlighting a zonation in the footwall, from a broad zone of rock deformed under amphibolite-facies conditions, through a narrowing zone of greenschist-facies mylonites, to the highly localized brittle Simplon Line (e.g. Campani et al., 2014; Mancktelow, 1985, 1987); detailed accounts of quartz microstructure, recrystallization mechanisms, and Ti-in-quartz contents as they vary with distance into the footwall (Haertel & Herwegh, 2014; Haertel et al., 2013); and thermochronology and thermokinematic modeling, which has provided estimates on the timing and rates of exhumation (Campani et al., 2010a, 2010b; Grasemann & Mancktelow, 1993).

Figure 1. a) Location of the study area, in the central European Alps. From Google Maps (accessed 2020). b) Geological setting of the SSZ. Adapted from Campani et al. (2010a) and the Tectonic Map of Switzerland (2005). A-A’ and B-B’ show the locations of the cross sections in Fig. 2. c) Stereoplots illustrating the moderate SW dip of both the earlier S_m and later S_{m2} foliations in the central part of the SSZ, and their associated down-plunge lineations.



2.2 Footwall Zonation

Due to progressive strain localization with exhumation and cooling, deformed rock in the footwall shows a transition structurally upwards from distributed deformation associated with peak amphibolite-facies metamorphism in the core of the Lepontine Dome, into a mylonite zone 1-2 km thick below the brittle fault, and then into a <10 m thick zone of cataclastic rocks and gouge along the brittle Simplon Line (Campani et al., 2010a; Mancel & Merle, 1987; Mancktelow, 1985). This zonation is reflected by quartz microstructures, syn-deformation retrograde alteration mineralogy, and mineral-chemistry thermometry, with Ti-in-quartz thermometry suggesting deformation temperatures of ~560°C deep in the footwall to ~350°C close to the brittle Simplon Line (Haertel et al., 2013). However, it is important to note that Haertel et al. (2013) assumed a constant a_{TiO_2} of 1 and pressure of 4 kbar to calculate these temperatures; a lower, variable a_{TiO_2} (as may be expected in metagranites lacking significant rutile) and deformation over a range of pressures (typical of an exhuming system) would affect

these estimates. Deformation occurred under relatively wet conditions (Mancktelow & Pennacchioni, 2004), with the synkinematic formation of quartz veins in the mylonitic footwall (Haertel et al., 2013).

2.3 Timing, Rate, and Amount of Exhumation

Fission track, $^{40}\text{Ar}/^{39}\text{Ar}$, and Rb/Sr dating provide constraints on the timing and rates of SSZ activity. Thermokinematic modeling of this data suggests that there was little relative displacement between footwall and hangingwall before ~18.5 Ma, during distributed ~NE-SW stretching (Campani et al., 2010b; Grasemann & Mancktelow, 1993). Thereafter, deformation localized onto the discrete, yet still broad, ductile SSZ, which between ~18.5 and ~14.5 Ma accommodated ~1 mm/year of footwall exhumation relative to the hangingwall (Campani et al., 2010b), although an earlier study suggested a faster exhumation rate (Grasemann & Mancktelow, 1993). Both studies agree that relative footwall exhumation slowed to ~0.35 mm/year at ~14.5 Ma, which continued until displacement ceased sometime between ~3 Ma and the present. In addition, erosion is modeled as exhuming both the hanging- and footwall by a constant ~0.36 mm/year. The total amount of footwall exhumation predicted by these models (~21-27 km) is consistent with peak metamorphic conditions of ~519-612°C and ~6.4-9.1 kbar in the core of the Toce Dome (Baxter & DePaolo, 2000; Vance & O’Nions, 1992), dated at ~32.5-29 Ma by garnet U-Pb and Rb-Sr geochronology (Vance & O’Nions, 1992).

3 Sampling

A total of 48 samples from two detailed transects (Fig. 2) were characterized in terms of their microstructure, and analyzed in order to estimate P-T-t conditions of deformation. The Gabi-Gondo and Zwischbergen transects are located in the central part of the SSZ, where consistently down-dip lineations indicate predominantly normal-sense motion throughout the preserved history of the SSZ (Fig. 1). The Gabi-Gondo transect extends from the brittle Simplon Line 7.6 km into the footwall (equivalent to 4.3 km structural distance from the ~30°-dipping fault), with excellent exposure provided along the Simplon Road (SS33) between the towns of Gabi and Varzo. Exposure approaches 100% along the upper several kilometers of the transect, with the exception of the area immediately adjacent to the brittle fault itself, which is obscured by the narrow, forested Diveria river gorge. Material was sampled from the metagranites of the Monte Leone nappe, located in the footwall immediately below the brittle fault, metagranites that occur with marbles and calc-schists of the structurally underlying Lebendun nappe, and the metagranites of the structurally-deepest Antigorio nappe. The Zwischbergen transect comprises a shorter but densely sampled section extending from the well-exposed brittle fault ~1.5 km into the footwall (~930 m structural distance). It comprises mostly Monte Leone nappe metagranites, with a small number of samples from the Lebendun and Antigorio metagranites. Exposure from the brittle fault through much of the Monte Leone nappe is excellent, occurring along the Grosses Wasser river upstream of a hydroelectric dam.

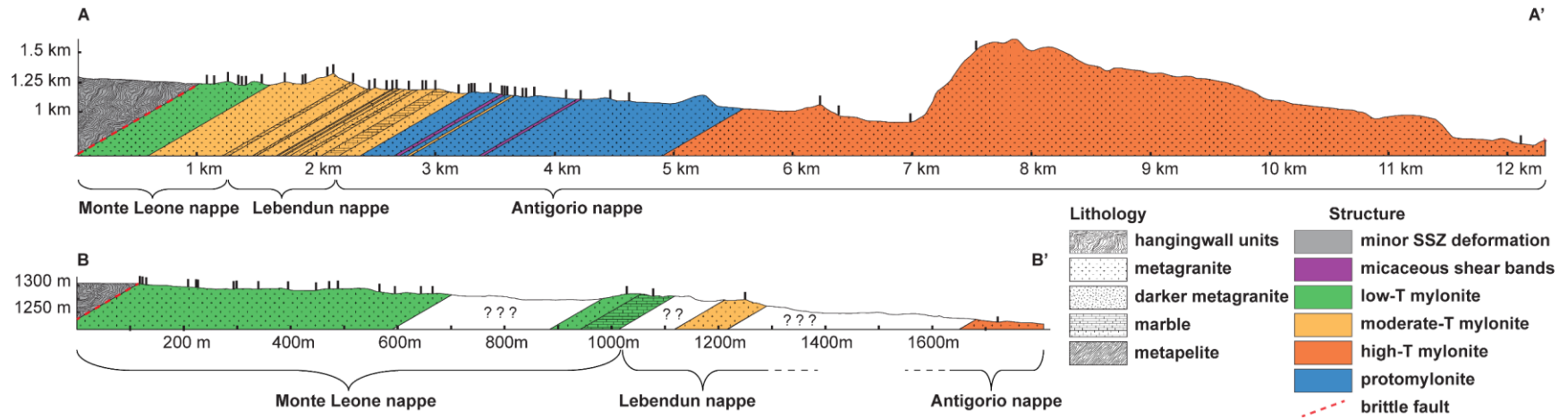


Figure 2. Cross sections through the Gabi-Gondo (A-A') and Zwischbergen (B-B') transects. See Fig. 1 for locations, and note the difference in scales. Black ticks indicate the locations of samples used in this study.

Along the studied transects, the metagranites comprise deformed granitic gneiss with variable proportions of quartz, plagioclase, alkali feldspar, and phengite, lesser but variable biotite and epidote, and minor to trace apatite, zircon and fine-grained Ti-bearing phases (predominantly titanite and micron-scale Ti-rich phases included in fine-grained phengite, with rare trace rutile). Most samples are feldspar-rich, but some contain abundant phengite and display a micaceous or phyllonitic fabric. Towards the brittle fault and in late cross-cutting shear bands, some samples display minor to moderate retrogression of biotite to chlorite. Amphibole has not been observed, and minor garnet has only been observed in rare, more mafic samples.

4 Methods and Results

4.1 Macro- and Microstructure

Microstructural observations were made using optical and backscatter electron (BSE) microscopy, and focused on deformation features such as dynamic recrystallization and syn-kinematic neocrystallization, the relation between quartz and phengite, and evidence for structural overprinting. Because microstructural control is essential for analyzing quartz-phengite pairs equilibrated simultaneously, all observations and analyses were made on the same polished 1-inch diameter round thin sections, cut perpendicular to the foliation and parallel to the lineation (in the XZ plane of finite strain). All analyzed locations were carefully located with the aid of optical cameras inside the various instruments, and recorded on high-resolution photomicrographs of each thin section (Fig. 3).

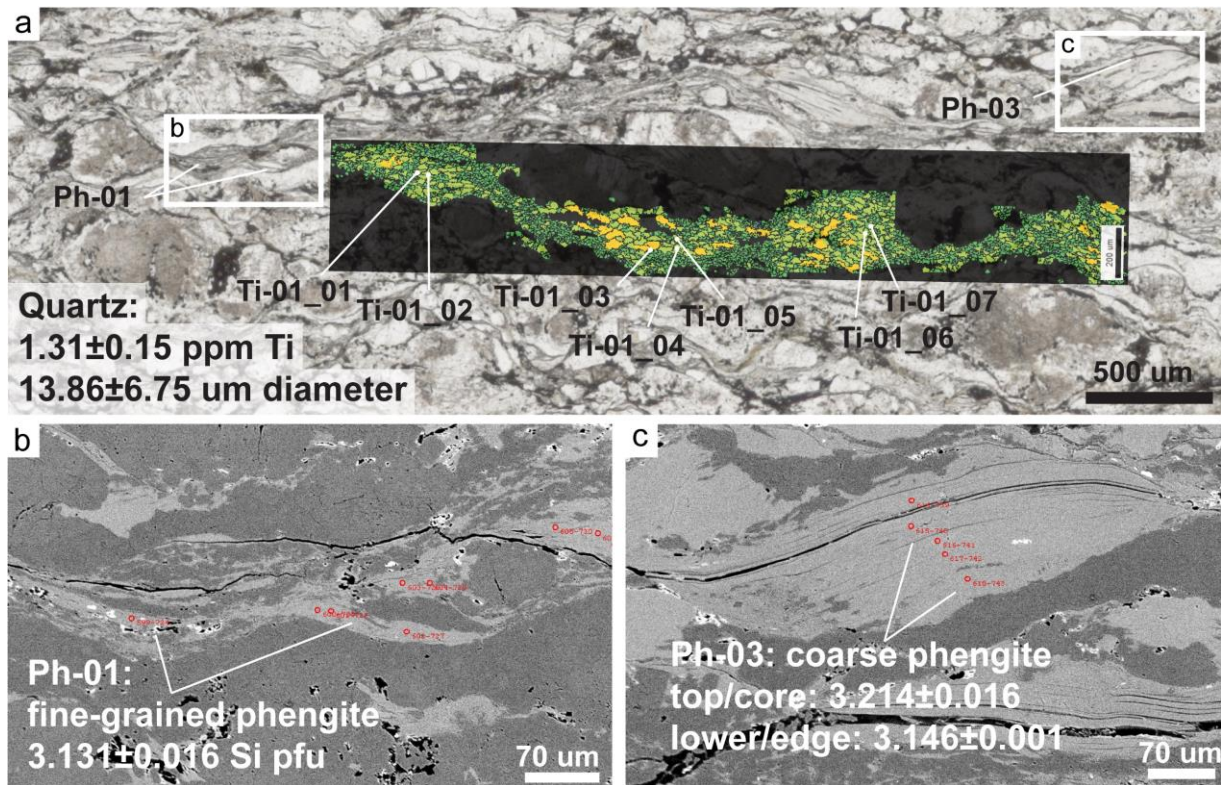


Figure 3. An example (sample TS-002) of the images on which all analytical locations were recorded. a) Photomicrograph in plane-polarized light, labelled with the positions of Ti-in-quartz

SIMS spot analyses, and overlain with an EBSD-derived map of recrystallized quartz grains, color coded by grain size (warmer colors = larger grains). White boxes show the locations of (b) and (c), BSE images on which the locations of Si-in-phengite microprobe spots were recorded.

4.1.1 Protomylonites

While the pre-SSZ protolith to the Monte Leone mylonites is not preserved in the study area, some sections of the Antigorio gneiss along the Gabi-Gondo transect display relatively weak deformation. These protomylonites have a coarse-grained, isotropic to weakly foliated texture, with cm-scale subhedral magmatic feldspar grains, some of which display Carlsbad twinning (Fig. 4, 5). Weak SSZ deformation entails undulose extinction in quartz; minor- to moderate dynamic recrystallization of quartz by subgrain rotation recrystallization (SGR) or transitional SGR/ unrestricted grain boundary migration (GBM); and the development of an incipient foliation defined by elongate quartz domains, weakly aligned biotite, and the breakdown of coarse feldspars into elongate lenses. Phengite is minor, and occurs as randomly-oriented, medium-grained laths associated with biotite, or as laths or anhedral patches within feldspar grains (Fig. 5).

4.1.2 Mylonites to Ultramylonites

The remainder of the samples comprise mylonitic- to ultramylonitic metagranite with moderate to intense SSZ-related strain. This is characterized by a moderate- to strong, gently SW-dipping foliation (S_m , sensu Campani et al., 2010a), a weak- to strong SW- or WSW-plunging lineation (L_m), and abundant down-dip normal-sense kinematic indicators (Fig. 4).

In the fault-distal portions of the transects, where higher-T deformation is preserved (“high-T mylonites” in Fig. 2), the S_m foliation is defined by weak gneissic compositional banding, smeared-out feldspar lenses, highly elongate quartz domains, and the preferred orientation of biotite and phengite laths (Fig. 5). Lineations are weak, while mm- to cm-scale feldspar sigma clasts indicate a normal shear sense. Relict feldspar porphyroclasts display subgrain development and recrystallization/disaggregation into medium-grained neoblasts. In high-strain samples, where the coarse igneous assemblage is no longer recognizable, much of the rock comprises pervasively intermixed quartz and medium-grained feldspar. This is interpreted as the final stage in the recrystallization/disaggregation of coarse igneous feldspar, and the intermixing of it with recrystallized quartz. Where present in quartz-only domains, or in deformed veins parallel to the foliation, quartz displays undulose extinction and coarse-grained transitional SGR/GBM-like microstructures. Elsewhere, quartz grains appear pinned by feldspar and mica. Phengite occurs as euhedral, medium-grained laths parallel to the foliation (Fig. 5).

Closer to the brittle fault, where moderate-T deformation overprints the high-T microstructures (“moderate-T mylonites” in Fig. 2), S_m is defined by finer compositional banding, with elongate trains of feldspar grains that appear to be the disaggregated remnants of larger porphyroclasts, and sub-mm quartz lenses that anastomose between feldspar grains, along with the preferred orientation of phengite laths (Fig. 4, 5). A well-developed, fine quartz stretching lineation is observed. Narrow (cm to sub-mm wide) quartz veins orientated parallel to the foliation become increasingly abundant towards the brittle fault. Quartz displays subgrain development and medium-grained SGR recrystallization. Medium-grained phengite laths occur in narrow, semi-continuous lenses that anastomose around feldspar porphyroclasts. In some samples, narrow rims of fine-grained phengite are developed along the edges of these larger

phengite laths, and appear closely associated with adjacent dynamically recrystallized quartz (Fig. 6).

Closest to the brittle fault, where lower-T deformation has overprinted all earlier microstructures (“low-T mylonites” in Fig. 2), the mylonites are finer grained. Feldspar-rich samples comprise abundant medium-grained feldspar porphyroclasts in a fine-grained matrix of quartz, feldspar, and phengite, with the foliation defined by elongated trains of feldspar porphyroclasts, narrow anastomosing quartz lenses, and narrow lenses of phengite (Fig. 5). Samples richer in phengite have a strong phyllonitic fabric defined by abundant coarse phengite laths. Small-scale shear bands are variably developed. These deflect the tails of feldspar sigma clasts and phengite mica fish, forming an S-C fabric consistent with SW-directed normal-sense shearing. These shear bands become increasingly well developed as the brittle fault is approached, until they merge to form a new, spaced foliation (S_{m2} , Fig. 4, 5). This younger, lower-T foliation dips more steeply than S_m , and is associated with fine quartz stretching lineations and rare minor chlorite. Quartz in foliation-parallel lenses and veins displays fine grained bulging recrystallization (BLG) to SGR. Phengite occurs as lenses of fine-grained material, along the foliation or shear bands, or around the edges of larger phengite- or feldspar porphyroclasts. These fine-grained masses may be rich in fine biotite and/or chlorite, and micron-scale Ti-rich inclusions (Fig. 6).

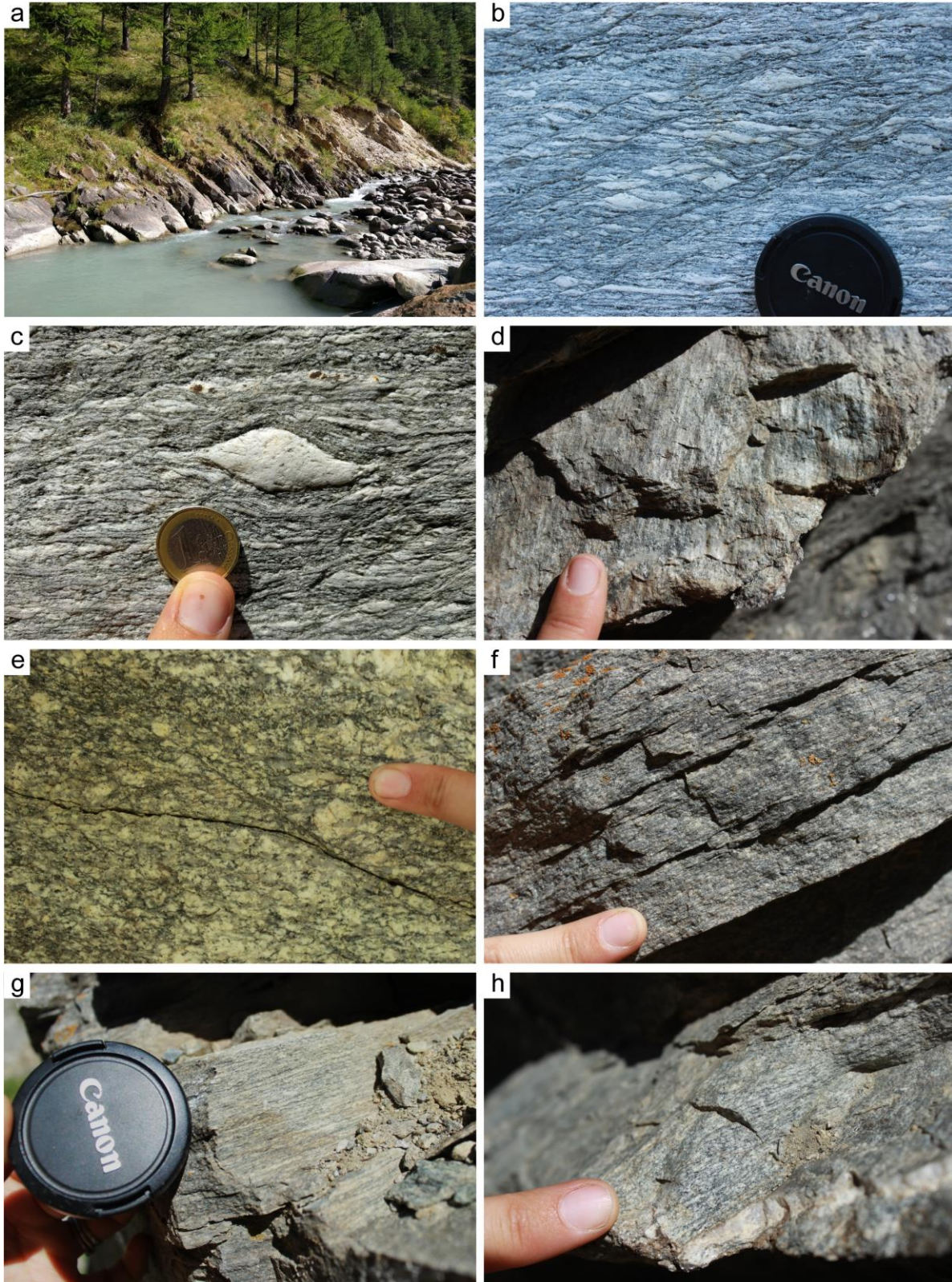
4.1.3 Departures from Zonation

Overall, the SSZ is characterized by a progressive zonation from high-T fabrics in the fault-distal footwall to low-T fabrics in the fault-proximal footwall. However, occasional departures from this trend do exist, in the form of both shear bands (sub-mm to m-scale, lower-T shear zones that cut rock displaying a significantly higher-T fabric) and the abovementioned sections of protomylonites.

Shear bands range from sub-mm to m-wide structures. The sub-mm shear bands occur as isolated structures or in m-scale clusters, and are most commonly observed in the high-T mylonitic gneiss or protomylonites of the distal Gabi-Gondo transect. They deflect or cut the existing foliation and are characterized by fine BLG±SGR recrystallization of quartz, fine-grained phengite, and occasional micron- to mm-scale brittle slip surfaces (Fig. 5). Some are chloritic, with well-developed, fine chlorite and/or quartz stretching lineations plunging SW. The m-scale shear bands cut the protomylonites, and exhibit near-complete replacement of feldspar by phengite (Fig. 5). They have a strong SW-dipping foliation, defined by alternating lenses of quartz and phengite. Quartz displays near-complete recrystallization by medium-grained SGR. Phengite occurs as coarse mica fish with undulose extinction, with minor fine-grained phengite along the edges of fish and as elongate tails, adjacent to recrystallized quartz. These shear bands are interpreted to have been associated with significant fluid flow, resulting in the hydration of feldspar to phengite.

Figure 4. Field photographs from the study area. a) The brittle fault (pale cream color) and immediate footwall (darker grey) on the Zwischbergen transect. b,c) Feldspar sigma clasts and incipient shear bands in moderate-T mylonites, indicating top-down-to-SW normal-sense motion. d) ~SW-plunging quartz stretching lineations in low-T mylonites. e) Coarse protomylonites with relict igneous feldspar crystals and a weakly developed foliation, cut by <mm-wide brittle-ductile shear bands. f,g) Moderate- to low-T mylonites exhibiting finer grain

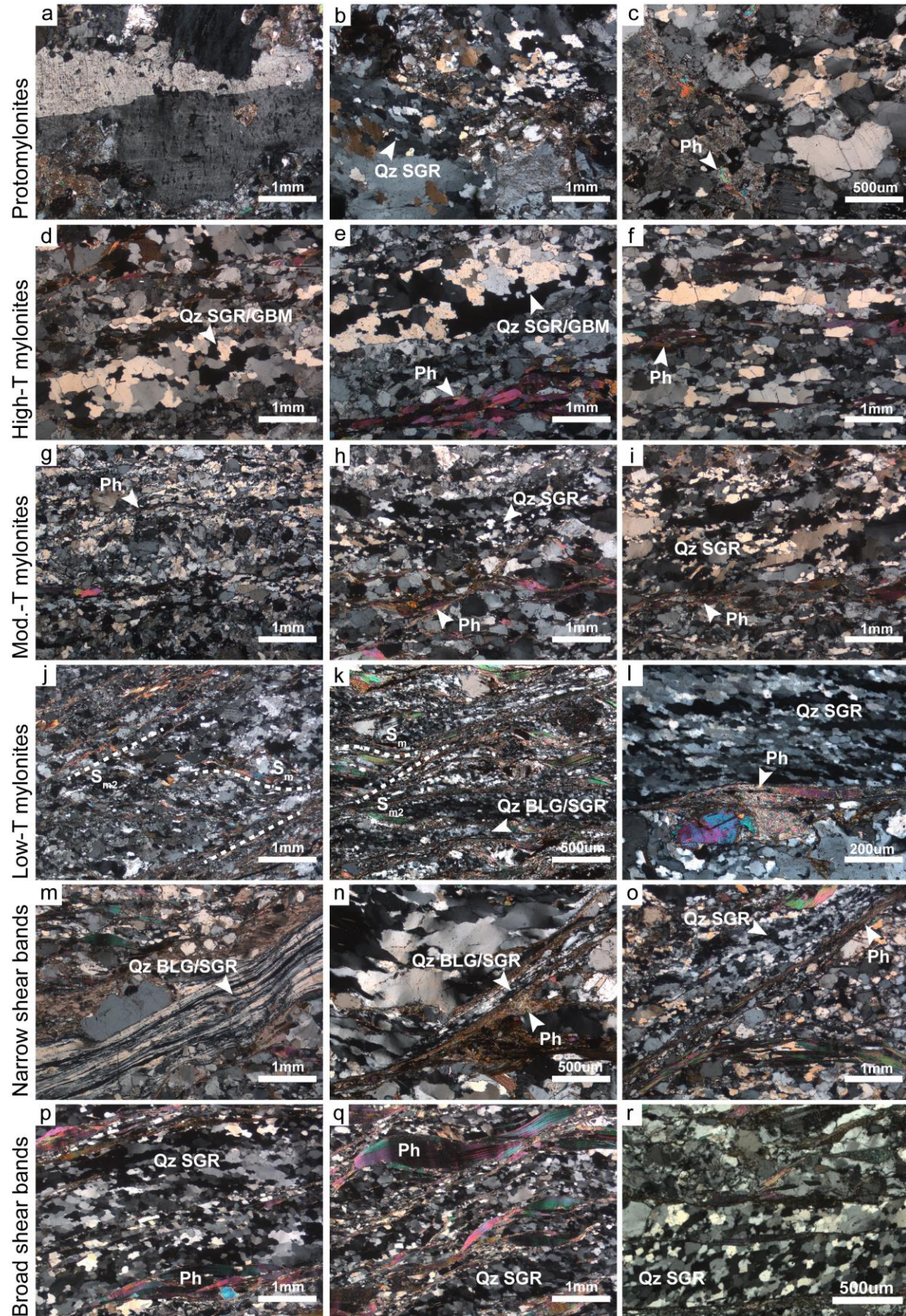
sizes and a well developed, planar S_m foliation. h) Low-T mylonite with a planar S_m foliation, curved into a spaced S_{m2} foliation, with fine quartz stretching lineations on the S_{m2} surface.



4.1.4 Overprinting and Composite Microstructures

It is important to note that much of the SSZ footwall has composite microstructures that reflect progressive overprinting at different conditions (Fig. 6). Only the most distal samples display exclusively high-T deformation, without any subsequent overprinting. It is therefore essential that the phases used for thermobarometry reflect deformation at the same time, under the same conditions. In samples with composite microstructures, this requires careful petrography.

Figure 5. Representative photomicrographs from the SSZ footwall, crossed polars. Protomylonites with relict igneous textures, and minor to moderate deformation: a) Carlsbad twin in a large magmatic feldspar; b) partial SGR recrystallization of coarse-grained, magmatic quartz; c) phengite formed from the breakdown of feldspar. High-T mylonites: d,e) pervasively deformed metagranite, with domains of coarse-grained quartz recrystallized by transitional SGR/GBM, disaggregated (recrystallized?) feldspar, and coarse laths of phengite defining a planar foliation; f) quartz grain size may be limited by other phases, with quartz occurring in narrow lenses or as isolated grains. Moderate-T mylonites: g) pervasively recrystallized quartz and feldspar, with feldspar-rich domains representing recrystallized porphyroclasts, outlined by biotite and phengite; h,i) lenses of medium-grained SGR-recrystallized quartz, and coarse phengite and biotite laths anastomosing between feldspar grains. Low-T mylonites: j,k) fine-grained BLG/SGR quartz in narrow, anastomosing lenses defining S_m (~horizontal), and finer BLG/SGR-recrystallized quartz and fine-grained phengite in narrow shear bands defining S_{m2} (dipping left); l) fine-grained SGR-recrystallized quartz in a vein parallel to S_m , with fine-grained phengite wrapping a bright epidote porphyroclast. Narrow shear bands cutting higher-T microstructures: m,n,o) fine-grained quartz recrystallized by BLG/SGR, and fine-grained phengite along discrete, narrow shear bands that dip more steeply than the earlier, higher-T S_m foliation. Broad, micaceous shear bands: p,q) alternating domains of medium-grained SGR-recrystallized quartz and coarse phengite laths, with mica fish displaying undulose extinction; r) although most feldspar in the broad shear bands has been replaced by white mica, relict feldspar is observed in some samples. Qz = quartz, Ph = phengite.



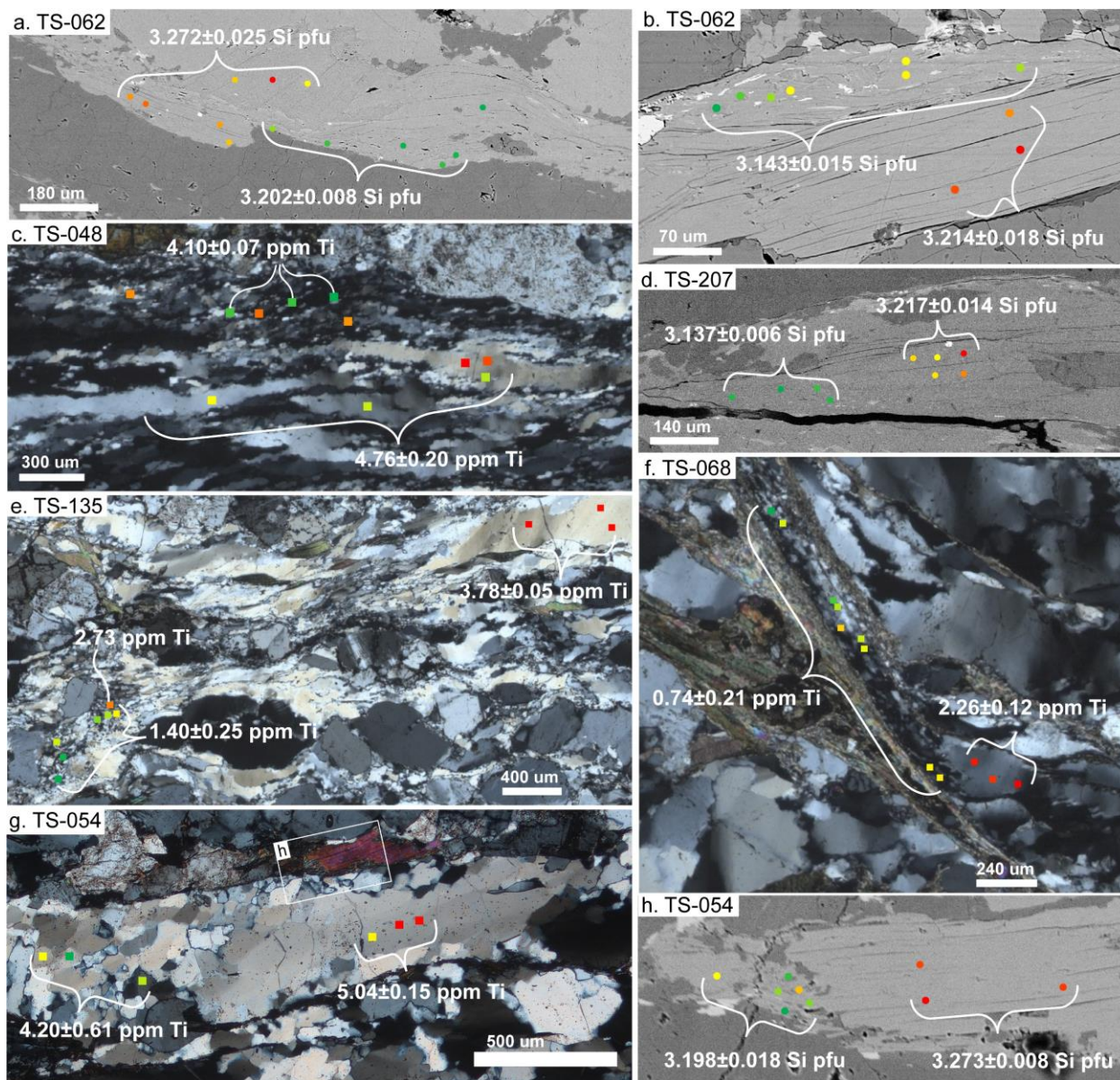


Figure 6. Relict quartz and phengite co-existing with finer-grained, younger quartz and phengite. Analytical spot positions are shown with circles (microprobe) or squares (SIMS), and colored according to their relative Si- or Ti-content (warmer colors = higher values). Images are photomicrographs taken in cross polarized light, unless otherwise stated. a,b) BSE images showing younger, fine-grained phengite with fine streaks of biotite and chlorite (pale grey) and Ti-rich phases (white), developed along the margins of older, coarser phengite with higher Si content. c) Dynamically recrystallized, Ti-poorer quartz adjacent to Ti-richer, relict ribbon quartz. d) A BSE image of fine-grained, Si-poorer phengite along the edge of relict, coarser, Si-richer phengite. e,f) Relict, coarse quartz with undulose extinction and higher Ti, and fine quartz recrystallized by BLG/SGR with lower Ti. g) Lower Ti values associated with subgrain development and SGR recrystallization in quartz. h) The adjacent coarse phengite lath displays fine-grained, Si-poorer phengite along its margin. BSE image.

4.2 Si-in-Phengite

Phengite is an intermediate member of the muscovite-celadonite $\text{KAl}_2[\text{AlSi}_3\text{O}_{10}](\text{OH})_2 - \text{K}(\text{Mg}, \text{Fe}^{2+})(\text{Fe}^{3+}\text{Al})[\text{Si}_4\text{O}_{10}](\text{OH})_2$ solid solution series. The strong pressure- and lesser temperature dependence of phengite composition has been experimentally demonstrated over a wide range of conditions (3-55 kbar, 350-1100°C) and compositions/assemblages, with a higher Si content per formula unit (pfu) at higher pressures and lower temperatures (Massonne & Schreyer, 1987; Massonne & Szpurka, 1997). Subsequent thermodynamic calculations have confirmed this P-T dependence (Coggon & Holland, 2002). At higher grades the relation breaks down, as the required limiting assemblage destabilizes; in particular, the disappearance of biotite from granitic compositions above 20 kbar causes the Si content of phengite to become insensitive to pressure (Massonne, 2015). Lower water activity in the bulk rock, the presence of Fe, or an increased paragonite (Na) component, will lower the Si content, although the effect of water activity is relatively minor (Massonne, 2015; Massonne & Schreyer, 1987). In contrast, higher F correlates with a higher Si content (Massonne & Schreyer, 1987). It is therefore important to take the bulk composition into account when using Si-in-phengite thermobarometry (Massonne & Szpurka, 1997).

Massonne and Schreyer (1987) noted that both experimental and natural phengite compositions appear to re-equilibrate sluggishly at new P-T conditions, and that its use as a thermobarometer is limited by its commonly-observed lack of equilibration: many rocks contain compositionally zoned phengites, or multiple generations of phengite with different Si contents (e.g. Santamaría-López et al., 2019). However, this can be a useful characteristic: if a specific generation of phengite can be reliably linked to another thermobarometrically-useful phase (such as garnet or quartz) representing local equilibrium at specific P-T-t conditions, that specific mineral pair can yield useful P-T information (Massonne, 2015).

4.2.1 Microprobe Analyses

The composition of phengite and biotite were analyzed in-situ with a Cameca SX-100 electron microprobe at the University of California Santa Barbara, using a 5 µm spot size, 15-20 KV accelerating voltage, 10 nA current, and a counting time of 20 seconds on-peak and 10 seconds background on either side. Approximately five or more spots were analyzed on each grain (where large enough), or on a single cluster of grains (where grains were too small), and the results averaged to give a single composition with standard deviation for each phengite grain/cluster. Mineral formulae were calculated according to Deer et al. (2013), and Si content is reported as Si pfu, normalized to 11 O.

Individual spots with significantly higher Al, Ti, Mn, Na, Mg, Fe, Ca, Cr, or K are interpreted as having hit inclusions and excluded; to identify spots that hit quartz, outliers with significantly higher Si content were excluded. As an additional check, measured Si was plotted against Al+Mg+Fe. Analyses of pure white mica are expected to fall on a straight line, representing muscovite-celadonite solid solution, and any spots that deviate significantly were considered contaminated and excluded.

Backscatter electron (BSE) imaging, along with X-ray mapping and semi-quantitative spot analyses by energy-dispersive X-ray analysis (EDS), was conducted on a Tescan Vega-3 XMU scanning electron microscope (SEM) at the University of California Los Angeles, to identify compositional populations within samples and zonations within grains. Because a number of samples contain multiple phengite populations, and some samples contain zoned phengite (typically the older, coarse grains), care was taken to use phengite in direct contact with

dynamically recrystallized quartz, interpreted to have been deformed simultaneously. In addition, using the average composition of several spots from different parts of large grains, or within clusters of fine grains, allows any natural zonations to be encompassed in the stated standard deviation of the population.

4.2.2 Results

Results are available in Cawood and Platt (2020a) and summarized in Table 1, as the average Si pfu of each population. The Si content ranges from 3.069 to 3.290 pfu, with the highest Si in relict, coarse-grained phengite, and the lowest in fine-grained phengite associated with dynamically recrystallized quartz, and commonly hosting micron-scale Ti-phase inclusions. In samples with multiple phengite populations, the older, coarser grains typically have higher Si contents than the younger, finer populations (Fig. 6), suggesting the latter grew or equilibrated at different conditions.

4.3 Ti-in-Quartz

The temperature dependance of the Ti content of quartz (TitaniQ) was experimentally calibrated by Wark and Watson (2006), and subsequent experiments have quantified a lesser pressure dependence (Huang & Audetat, 2012; Thomas et al., 2010). We use the Ti-in-quartz thermobarometer calibration of Thomas et al. (2010), because it takes both pressure and a_{TiO_2} into account; subsequent experiments have confirmed the reproducibility of those used for calibration (Thomas et al., 2015); and it is widely used (e.g. Ackerson et al., 2018; Ashley & Law, 2015; Ashley et al., 2013; Cavalcante et al., 2018; Grujic et al., 2020; Menegon et al., 2011), allowing our data to be compared to that in the literature. However, we note that debate regarding calibrations for the Ti-in-quartz thermobarometers is ongoing (see, for example, discussion in Nachlas & Hirth, 2015), and some have suggested that temperatures derived using the Thomas et al. (2010) calibration appear too low (Ashley et al., 2013, 2014; Grujic et al., 2011).

It is important for this study that the P-T conditions indicated by the quartz Ti content reflect those of deformation, and not of the original magmatic or hydrothermal quartz formation. Since the first application of TitaniQ to quartz mylonites (Kohn & Northrup, 2009), numerous studies on both experimental and natural materials have found that dynamic recrystallization of out-of-equilibrium quartz resets its Ti content (e.g. Grujic et al., 2011; Haertel et al., 2013; Nachlas & Hirth, 2015; Nachlas et al., 2014, 2018). Of these, the earlier studies suggested that only recrystallization by GBM fully resets the Ti content (Grujic et al., 2011; Haertel et al., 2013), while later work advocates that BLG, SGR, and GBM are all able to reset it, at least partially (Ashley et al., 2014; Nachlas et al., 2014, 2018). Furthermore, Ti-in-quartz appears to be more readily reset by retrograde deformation, during which Ti is expelled from the recrystallizing material, and less easily reset during prograde recrystallization that requires Ti uptake (Negri et al., 2014). This may explain the failure of Grujic et al. (2011)'s lower-T SGR- and BLG-samples to have re-equilibrated during short-duration, prograde heating by contact metamorphism, as these authors themselves noted.

4.3.1 SIMS Analyses

The Ti content of quartz was analyzed in-situ by secondary ion mass spectrometry (SIMS) on a Cameca IMS 6f at Arizona State University, using a spot size of $\sim 5 \mu\text{m}$ ($\sim 20 \mu\text{m}$ for several preliminary samples), current of ca. 2.2-3.5 nA, accelerating voltage of 9000 V, and

primary ion beam of $^{16}\text{O}^+$. Samples were coated in gold, and each spot was subjected to a 5 minute pre-sputter to remove surface contamination, and then analyzed for 25-30 cycles, during which the ^{27}Al , ^{30}Si , ^{40}Ca , ^{48}Ti , and ^{49}Ti were measured. The spectra were monitored to ensure that Ca and ^{48}Ti were resolved. Doped-glass standards from the University of Edinburgh (Gallagher & Bromiley, 2013) with known ^{48}Ti -concentrations of 0, 100, and 500 ppm were analyzed immediately before and after each session, and used to reduce the data. At least 5 spots were analyzed on each grain (where grains were large enough), or on a single area of recrystallized grains (where grains were too small), and the results averaged to give a single Ti-value for each population. The standard deviation for the spots in each population is reported, and reflects the natural variability; this value is consistently larger than the error on individual spots.

Contaminated spot analyses or individual cycles with anomalously low Si or high Al, Ca, or Ti were excluded. Samples were investigated with cathodoluminescence (CL), to distinguish different populations or zonations. Extremely faint to no luminescence was observed. However, care was taken to only use dynamically recrystallized quartz, in apparent microstructural equilibrium with analyzed phengite, for P-T determinations. Furthermore, using the average Ti-content of several spots from different areas within large grains, or within populations of small grains, allows any natural zonations to be encompassed in the stated standard deviation.

4.3.2 Results

Results are available in Cawood and Platt (2020b) and summarized in Table 1, and range from 0.711 to 6.625 ppm Ti. The lowest Ti values are observed in fine-grained (<25 μm diameter) dynamically recrystallized quartz with an SGR or transitional BLG/SGR microstructure, within fault-proximal mylonites and narrow cross-cutting shear bands. The highest values occur in relict, coarse (>120 μm) grains or ribbons. Dynamically recrystallized quartz typically has a lower Ti-content than unrecrystallized, relict grains, and younger recrystallized populations typically have lower Ti than the older recrystallized populations they overprint (Fig. 6).

4.4 Geochemical Modeling

4.4.1 Bulk Rock Composition by XRF

Bulk-rock composition was analyzed by X-ray Fluorescence (XRF) at the California Institute of Technology, using a 4 kW Zetium Panalytical analyzer. Samples were prepared by manually removing any late cross-cutting veins and weathered rinds before crushing a representative quantity of rock between sheets of thick plastic, and grinding in an agate mill. All metal was avoided during the preparation process to minimize the risk of Ti contamination. Powdered samples were dried before determining loss on ignition (LOI), and then fused with a LiT/LiM/LiI flux to create glass pellets for XRF analysis. The USGS standards RGM-2 (rhyolite) and GSP-2 (granodiorite) yielded compositions comparable to their accepted values. All samples yielded totals between 98.9 and 100.4 wt%, including trace elements. Data is available in Cawood and Platt (2020c).

Table 1. Analytical Results and Calculated Conditions of Deformation.

	Sample	Microstruc. setting*	Phengite Si (pfu)			Quartz Ti (ppm)			T of deformation (°C)			P of deformation (kbar)			a _{TiO2}	Age (Ma)
			avg	1 SD	n	avg	1 SD	n	best est.	2 SD max.	2 SD min.	best est.	2 SD max.	2 SD min.		
Gabi-Gondo	TS-281	latest	3.170	0.005	5	1.436	0.187	8	361.7	379.8	339.5	2.22	2.67	1.66	0.33	13.4
	TS-281	shear band	3.162	0.007	9	0.711	0.049	5	324.0	335.4	311.5	1.57	1.95	1.21	0.28	11.5
	TS-048	latest	3.212	0.019	10	2.865	0.302	5	423.5	458.0	390.1	3.95	5.45	2.68	0.35	18.4
	Ti-049	shear band	3.147	0.017	7	1.494	0.057	4	351.7	374.9	317.3	1.60	2.63	0.55	0.33	12.9
	TS-192	latest	3.149	0.011	8	1.976	0.429	5	369.0	399.7	322.9	1.86	2.73	ca. 0.71	0.35	13.4
	TS-193	latest	3.137	0.010	4	3.554	0.311	8	384.2	403.4	362.9	1.79	2.50	1.06	0.45	14.1
	TS-195	latest	3.142	0.008	5	1.243	0.119	6	337.0	357.6	318.9	1.29	2.35	ca. 0.57	0.33	12.3
	TS-196	latest	3.146	0.016	12	1.550	0.133	5	342.4	369.6	313.1	1.38	2.46	0.49	0.39	12.4
	TS-196	relict	3.290	0.031	4	2.042	0.242	6	442.6	466.9	385.4	7.58	ca. 11.0	3.58	0.55	ca. 22
	TS-279	latest	3.175	0.022	9	1.388	0.437	7	357.6	412.6	274.9	2.63	5.56	ca. 0.32	0.39	13.2
	TS-051	shear band	3.193	0.021	5	2.505	0.556	5	368.0	408.8	318.7	2.86	4.23	1.42	0.62	13.8
	TS-051	latest	3.235	0.018	3	3.908	0.147	5	413.7	436.0	390.8	4.33	5.34	3.29	0.65	18
	TS-216	latest	3.143	0.008	15	3.351	0.496	7	389.2	408.9	361.8	2.12	2.72	1.37	0.30	14.75
	TS-059	latest	3.126	0.013	7	3.466	0.325	5	376.8	399.2	346.1	1.50	2.33	0.44	0.45	13.8
	TS-202	latest	3.171	0.008	10	3.246	0.057	5	405.4	418.2	394.4	2.85	3.42	2.37	0.38	16.4
	TS-054	latest	3.143	0.012	4	4.002	0.550	6	396.5	419.5	369.6	2.18	3.04	1.32	0.48	14.75
	TS-054	relict	3.198	0.018	6	4.203	0.606	3	433.4	468.1	396.8	3.96	5.48	2.59	0.45	19.1
	TS-054	relict	3.273	0.008	3	5.044	0.147	3	490.2	502.3	476.4	6.73	7.30	6.09	0.50	ca. 24.5
	TS-205	latest	3.147	0.006	6	2.715	0.185	5	376.8	390.6	361.6	2.04	2.46	1.59	0.43	13.8
	TS-060	latest	3.180	0.014	4	5.123	0.130	7	429.2	447.1	406.7	3.54	4.49	2.52	0.48	19
	TS-061	latest	3.117	0.015	4	2.969	0.679	9	364.9	398.4	299.9	1.14	2.24	ca. 0.08	0.44	13.2
	TS-062	relict	3.202	0.008	6	2.957	0.089	2	418.9	432.0	405.4	3.69	4.26	3.14	0.38	18
	TS-062	latest	3.143	0.015	7	3.820	0.149	3	392.0	414.2	366.3	2.07	3.04	1.01	0.48	14.6
	TS-207	relict	3.150	0.006	6	4.217	0.760	7	397.4	416.1	373.7	2.21	2.74	1.66	0.48	14.7
	TS-207	latest	3.138	0.005	5	4.081	0.284	5	387.7	399.5	375.5	1.81	2.21	1.42	0.49	14.5
	TS-208	latest	3.139	0.009	5	4.107	0.299	6	390.2	409.1	372.5	1.91	2.64	1.28	0.49	14.6
	TS-064	latest	3.166	0.015	3	3.773	0.304	5	406.2	432.0	379.9	2.71	3.83	1.71	0.45	16.5
	TS-065	shear band	3.140	0.008	5	3.182	0.452	7	385.7	404.1	363.9	1.99	2.55	1.40	0.43	14.4
	TS-209	latest	3.134	0.016	9	4.187	0.638	7	388.6	419.3	353.5	1.83	2.95	0.66	0.50	14.5

	TS-066	latest	3.215	0.029	6	2.857	0.301	5	419.4	467.7	371.3	3.77	5.94	1.91	0.37	18
	TS-210	latest	3.182	0.014	9	3.084	0.258	4	336.4	359.5	316.9	1.81	2.74	1.15	1.00	12.2
	TS-211	latest	3.134	0.007	8	4.382	0.491	8	391.4	407.6	373.0	1.90	2.47	1.34	0.51	14.6
	TS-067	latest	3.222	0.014	6	3.628	0.676	5	444.0	476.9	406.7	4.66	5.99	3.41	0.40	20.5
	TS-033	latest	3.135	0.010	4	4.969	0.787	7	393.3	418.3	368.5	1.84	2.69	1.11	0.55	14.9
	TS-068	shear band	3.126	0.016	14	0.735	0.212	9	300.3	344.3	231.9	0.74	1.76	ca. 0	0.36	11.9
	TS-034	latest	3.147	0.016	5	4.790	0.556	10	399.5	428.1	370.2	2.18	3.31	1.10	0.53	15
	TS-069	latest	3.163	0.012	6	3.906	0.427	8	407.9	427.5	383.6	2.78	3.52	1.92	0.45	17.1
	TS-170	latest	3.187	0.025	6	6.625	0.477	7	440.0	479.6	399.6	3.80	5.68	2.01	0.58	> ca. 21
Zwischbergen	TS-011	latest	3.169	0.028	16	1.873	0.113	6	377.2	414.4	324.6	2.39	3.97	0.49	0.32	13.9
	TS-131	latest	3.146	0.012	4	1.827	0.083	4	361.6	379.6	331.9	1.71	2.39	0.66	0.35	13.2
	TS-002	latest	3.131	0.016	11	1.314	0.147	5	320.4	346.1	296.7	1.19	2.03	0.40	0.49	11.5
	TS-134	latest	3.127	0.010	6	2.754	0.154	3	367.0	385.1	348.1	1.40	2.10	0.71	0.45	13.4
	TS-134	relict	3.134	0.020	5	3.575	0.215	3	383.4	413.3	345.6	1.77	3.06	0.31	0.46	14
	TS-133	latest	3.160	0.010	8	1.521	0.224	12	358.6	383.8	330.0	2.06	2.82	1.28	0.34	13.1
	TS-135	latest	3.170	0.008	13	1.400	0.246	6	355.0	384.2	330.8	2.34	3.06	1.75	0.37	13
	TS-135	relict	3.190	0.011	7	3.776	0.047	3	425.7	443.6	410.1	3.77	4.59	3.05	0.43	18
	TS-013	latest	3.069	0.026	10	2.772	0.252	5	326.85	373.7	246.85	0.13	1.74	ca. 0	0.60	11.5
	TS-014	latest	3.153	0.010	5	3.485	0.339	6	399.8	427.3	376.2	3.34	4.82	2.16	0.55	15.5
	TS-136	latest	3.159	0.016	8	1.686	0.226	5	303.7	325.3	279.8	1.51	2.20	0.82	1.00	11.3
	TS-137	latest	3.107	0.018	8	1.988	0.133	8	336.7	371.7	313.9	0.58	2.41	ca. 0.06	0.41	11.9
	TS-138	latest	3.110	0.017	12	2.518	0.332	5	360.6	394.7	316.4	1.17	2.39	0.13	0.41	13.2
	TS-241	latest	3.094	0.020	11	1.910	0.186	4	317.6	346.6	286.9	0.24	1.44	ca. 0	0.53	11.5
	TS-242	latest	3.162	0.016	11	1.967	0.077	6	380.4	402.9	357.0	2.51	3.46	1.50	0.34	14.1
	TS-139	latest	3.135	0.012	9	1.802	0.276	8	349.9	379.5	330.9	1.24	2.18	ca. 0.65	0.34	12.9
	TS-243	shear band	3.149	0.009	17	1.827	0.240	5	357.0	380.9	333.2	1.78	2.52	1.17	0.39	13
	TS-017	latest	3.144	0.022	9	1.846	0.293	7	358.6	399.8	298.9	1.62	3.11	0.18	0.37	13.2
	TS-031	latest	3.123	0.011	4	2.841	0.125	8	370.0	385.5	346.5	1.35	2.02	0.52	0.41	13.4

Note. abbreviations: avg = average, SD = standard deviation, n = number of analytical spots. Where T or P values fell outside of the modeled P-T space, they are given as approximate. See Table 2 for IGSN numbers.

* Latest = latest pervasive deformation, relict = relict pervasive deformation, shear band = narrow cross-cutting shear band.

4.4.2 Pseudosection Modeling Parameters

Using the bulk rock compositions, P-T phase diagrams (pseudosections) were generated for each sample using Perple_X (Connolly, 2005, version 6.8.3, source updated 12 June 2018, downloaded from perplex.ethz.ch on 13 June 2018) for the range 0.1 or 1-9 kbar and 100-700°C and the system $\text{SiO}_2\text{-TiO}_2\text{-Al}_2\text{O}_3\text{-MgO-MnO-FeO-Fe}_2\text{O}_3\text{-CaO-Na}_2\text{O-K}_2\text{O-H}_2\text{O}$. The measured bulk-rock chemistry was adjusted to match this 11-component system by a) reducing CaO according the assumption that all measured P, together with the corresponding amount of CaO, was bound in ideally-composed apatite; and b) recalculating the measured FeO content, so that 4-5% of the measured Fe was presented as Fe_2O_3 . This resulted in the modelled mineral assemblages better reflecting the observed assemblages, most of which contain epidote but lack magnetite or hematite. The adjusted compositions are provided in Table 2.

We used the thermodynamic dataset of Holland and Powell (1998) as revised in 2004 (database *hp04ver.dat*), together with the CORK fluid equation of state for water (Holland & Powell, 1991), and the following solution models: Chl(HP) for chlorite (Holland et al., 1998); Pl(h) (Newton et al., 1980) and San (Waldbaum & Thompson, 1968) for feldspar; Pheng(HP) for potassic phengite, restricted to allow a maximum of 50 mol% paragonite component (Powell & Holland, 1999); Mica(M) for sodic phengite, restricted to allow a maximum of 50 mol% phengite component (Massonne, 2010); Bio(HP) for biotite (Powell & Holland, 1999); and Ep(HP) for epidote, and the ideal mixing model IlGkPy for ilmenite (Holland & Powell, 1998).

Saturation with pure H_2O was assumed, with no CO_2 . Water saturation is a valid assumption for samples closer to the brittle fault, where quartz veins are abundant and the mineral assemblage involves hydrous retrograde phases such as phengite and chlorite, and is supported by previous studies (Haertel et al., 2013; Mancktelow & Pennacchioni, 2004). However, it is uncertain if this assumption is valid for samples further into the footwall, where veins are rare and a high-T assemblage is preserved. The assumption of a pure H_2O fluid is considered valid because minor calcite-bearing veinlets are typically only observed very close to the brittle fault.

Table 2. Bulk Rock Composition from XRF.

Sample	IGSN	SiO_2	TiO_2	Al_2O_3	FeO*	Fe_2O_3^*	MnO	MgO	CaO*	Na_2O	K_2O	LOI
Gabi-Gondo												
TS-281	IETKC0001	70.476	0.323	14.779	2.209	0.129	0.056	0.972	1.279	3.961	4.039	1.135
TS-048	IETKC0002	73.178	0.233	13.431	1.549	0.091	0.037	0.616	1.228	3.528	4.029	1.201
TS-049	IETKC0003	70.680	0.336	14.849	2.248	0.131	0.058	1.059	1.557	3.679	4.026	1.025
TS-192	IETKC0004	66.054	0.424	15.008	3.126	0.183	0.010	1.473	2.914	3.051	3.758	3.240
TS-193	IETKC0005	64.115	0.424	18.111	3.282	0.192	0.008	1.261	1.626	4.545	4.533	1.349
TS-195	IETKC0006	63.534	0.608	16.103	4.464	0.261	0.017	2.549	3.370	3.235	3.466	1.391
TS-196	IETKC0007	76.490	0.236	12.067	1.747	0.102	0.035	1.047	0.487	2.362	3.215	1.627
TS-279	IETKC0008	65.652	0.602	15.978	4.167	0.244	0.074	1.935	1.668	2.595	4.124	1.841
TS-051	IETKC0009	72.738	0.292	13.147	1.782	0.104	0.040	0.647	0.254	0.817	6.468	1.910
TS-216	IETKC000A	72.354	0.262	14.257	1.902	0.111	0.060	0.555	0.776	3.456	4.396	1.105
TS-059	IETKC000B	71.485	0.268	13.588	1.885	0.110	0.070	0.807	1.344	3.027	4.813	1.552
TS-202	IETKC000C	71.219	0.217	14.501	1.711	0.100	0.071	0.636	1.925	3.392	4.136	1.174

TS-054	IETKC000D	74.573	0.183	13.296	1.333	0.078	0.052	0.386	0.809	4.621	2.875	1.083
TS-205	IETKC000E	75.471	0.139	12.818	1.253	0.073	0.046	0.343	0.336	2.841	5.090	0.827
TS-060	IETKC000F	72.431	0.306	13.804	1.810	0.106	0.042	0.436	0.475	2.923	5.444	1.141
TS-061	IETKC000G	76.027	0.154	11.900	1.086	0.064	0.032	0.396	0.599	2.313	5.703	1.036
TS-062	IETKC000H	70.587	0.275	15.114	1.540	0.090	0.037	0.644	0.660	3.060	5.318	1.430
TS-207	IETKC000I	76.106	0.173	12.579	1.388	0.081	0.034	0.753	1.088	3.316	2.769	1.042
TS-208	IETKC000J	73.404	0.263	13.716	1.429	0.084	0.044	0.602	1.194	3.792	3.772	0.728
TS-064	IETKC000K	75.546	0.159	12.915	0.978	0.057	0.030	0.486	0.813	4.114	2.362	1.177
TS-065	IETKC000L	74.185	0.161	13.519	1.274	0.074	0.038	0.313	1.174	3.318	4.694	0.734
TS-209	IETKC000M	74.715	0.245	13.153	1.590	0.093	0.057	0.499	1.018	3.375	4.340	0.575
TS-066	IETKC000N	76.282	0.111	13.149	0.797	0.047	0.003	0.729	0.306	2.364	5.171	1.120
TS-210	IETKC000O	79.980	0.154	10.963	0.834	0.029	0.011	0.944	0.049	0.272	4.259	1.711
TS-211	IETKC000P	74.288	0.182	13.381	1.428	0.084	0.058	0.460	0.967	3.583	4.059	0.736
TS-067	IETKC000Q	75.490	0.125	12.396	0.957	0.056	0.037	0.237	1.281	3.333	4.214	1.119
TS-033	IETKC000R	70.709	0.397	14.360	2.271	0.133	0.063	0.856	1.814	3.611	3.601	1.358
TS-068	IETKC000S	74.953	0.265	12.408	1.736	0.102	0.039	0.745	0.903	3.009	4.243	0.711
TS-034	IETKC000T	76.615	0.155	12.380	1.384	0.081	0.032	0.704	1.331	3.561	2.757	0.703
TS-069	IETKC000U	72.040	0.238	14.412	1.691	0.099	0.053	0.545	1.667	3.744	3.822	0.866
TS-170	IETKC000V	72.892	0.218	14.288	1.613	0.094	0.005	0.548	1.092	3.932	3.727	0.913
Zwischbergen												
TS-011	IETKC000W	68.830	0.323	13.920	2.238	0.131	0.007	1.055	2.154	2.678	4.256	4.040
TS-131	IETKC000X	61.716	0.570	14.892	3.799	0.222	0.092	2.619	3.115	0.742	4.707	6.893
TS-002	IETKC000Y	71.337	0.317	15.241	1.897	0.111	0.032	0.338	0.446	3.815	4.309	1.395
TS-134	IETKC000Z	67.359	0.957	13.720	4.766	0.279	0.088	1.410	1.825	3.258	3.667	1.094
TS-133	IETKC0010	69.001	0.342	15.896	2.182	0.128	0.038	0.568	0.899	2.549	5.704	1.868
TS-135	IETKC0011	74.859	0.189	12.903	1.381	0.081	0.043	0.188	0.457	3.067	4.734	0.877
TS-013	IETKC0012	58.696	0.709	17.899	5.132	0.300	0.094	3.446	4.133	3.584	3.080	2.021
TS-014	IETKC0013	68.842	0.465	14.666	3.480	0.204	0.013	1.952	1.866	2.218	3.055	2.398
TS-136	IETKC0014	75.160	0.240	12.797	2.004	0.117	0.042	0.607	0.103	1.224	5.084	1.838
TS-137	IETKC0015	65.256	0.642	17.520	3.331	0.195	0.057	1.119	1.807	2.476	4.245	2.642
TS-138	IETKC0016	76.604	0.045	12.255	0.641	0.038	0.013	0.042	0.349	2.219	6.599	0.622
TS-241	IETKC0017	62.439	1.010	16.942	5.736	0.335	0.087	1.619	1.459	1.940	3.888	2.668
TS-242	IETKC0018	74.384	0.080	14.124	0.696	0.041	0.013	0.086	0.487	3.731	5.542	0.528
TS-139	IETKC0019	63.775	0.693	16.220	4.386	0.257	0.096	2.616	1.992	3.237	4.242	1.310
TS-243	IETKC001A	69.954	0.598	14.735	3.326	0.195	0.058	0.703	1.119	2.598	4.002	1.606
TS-017	IETKC001B	73.200	0.210	13.314	1.534	0.090	0.047	0.671	0.709	2.995	5.316	1.137
TS-031	IETKC001C	75.022	0.216	12.292	1.634	0.096	0.034	0.507	1.119	3.570	3.459	0.986

*Note that FeO, Fe₂O₃, and CaO have been adjusted to account for the presence of apatite and the occurrence of some iron as Fe³⁺, as described in the text.

4.4.3 Pseudosection Modeling Results

Selected pseudosections are shown in Figure 7. The pseudosections for all samples are similar, with quartz, feldspar, phengite, biotite, epidote, and titanite stable at moderate T (~280-400°C) and a wide range of P (~1-7.5 kbar). Phengite is stable over most of the investigated P-T range for the majority of samples, being present in lawsonite-jadeite-bearing assemblages at low T and high P, and feldspar-biotite-epidote assemblages at moderate P-T, but disappearing from feldspar-biotite-aluminosilicate assemblages at high T. Ti-rich phases include rutile at low P-T and again at moderate-high T, titanite (sphene) over a broad range of low- to moderate P-T, and

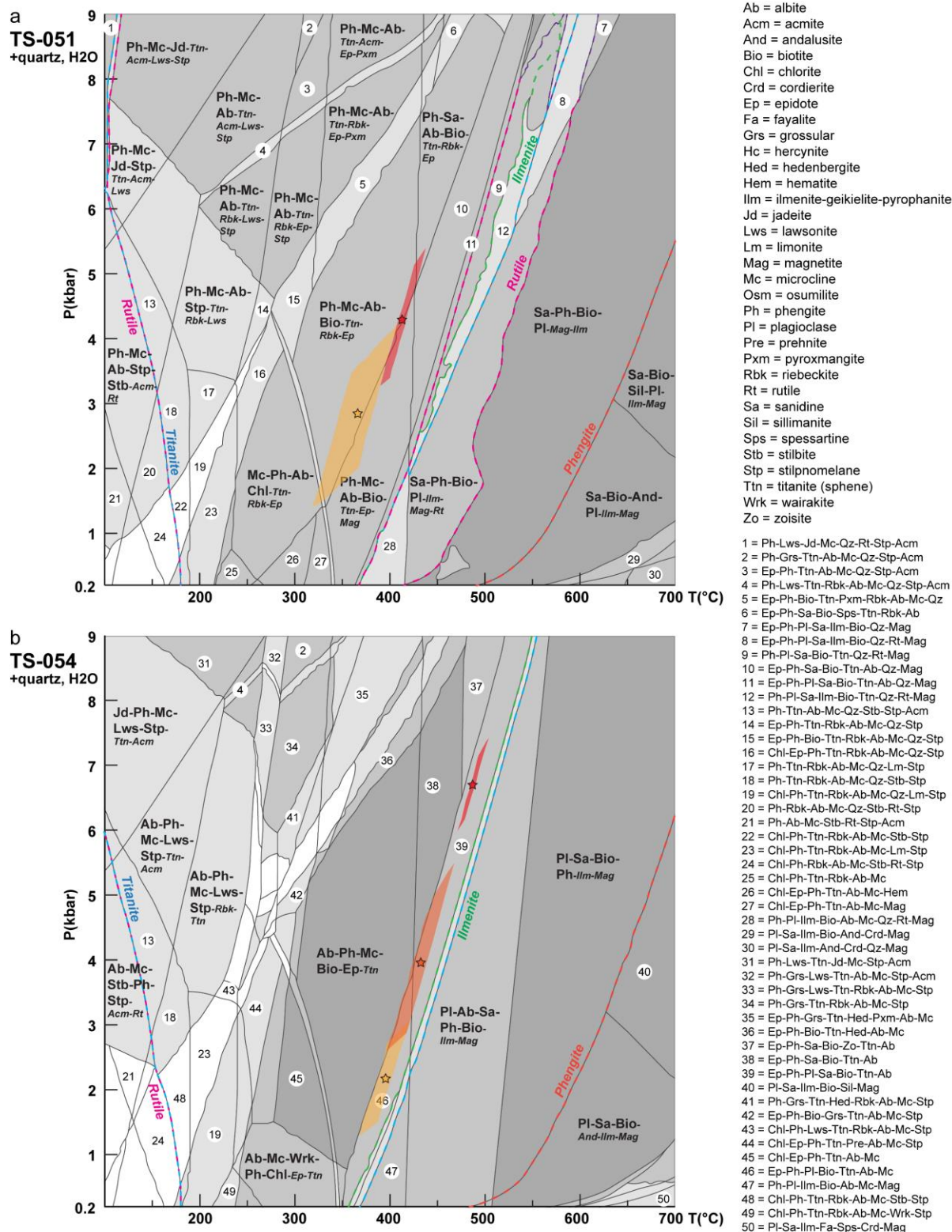
ilmenite at moderate- to high T. Note that the Pheng(HP) solution model for potassic white mica does not include Mn, which may occur in natural phengites; the pyroxmangite that is predicted by the models is not observed in our samples, and likely reflects the model's response to this "excess" Mn (Massonne, 2015). The same may be true for the modeled riebeckite.

4.4.4 Calculating Ti-in-Quartz and Si-in-Phengite Isopleths

In addition to pressure and temperature, the Ti-in-quartz thermobarometer is dependent on a_{TiO_2} (Thomas et al., 2010; Wark & Watson, 2006). Previous studies have assumed bulk rock a_{TiO_2} based on the presence of Ti-bearing accessory phases: $a_{\text{TiO}_2} = 1$ in the presence of rutile or anatase (Ghent & Stout, 1984; Haertel et al., 2013), $a_{\text{TiO}_2} = 0.7$ with ilmenite (Menegon et al., 2011), or $a_{\text{TiO}_2} = 0.8$ or 0.95 in ilmenite-bearing metapelites and amphibolites respectively (Chambers & Kohn, 2012). However, a_{TiO_2} may vary drastically as a function of bulk composition and mineral assemblage (Ashley & Law, 2015). We therefore model a_{TiO_2} for each sample in *Perple_X* using our bulk rock chemistry, according to the method outlined by Ashley and Law (2015). This allows us to calculate a_{TiO_2} for our full range of modeled P-T conditions, illustrated by isopleths in Figure 8a. Using the calibration of Thomas et al. (2010), we then use these a_{TiO_2} values to calculate equilibrium Ti-in-quartz values over the full P-T range (Fig. 8b). Isopleths of constant Si-in-phengite content are illustrated in Figure 8c, extracted directly from the Pheng(HP) solution model (e.g. Massonne, 2015).

The P-T dependence of Si in phengite, and of Ti in quartz, is clearly visible in Figure 8. Titanium activity is ~ 1 when rutile is stable, is lower in the high-T region of ilmenite stability, and is highly variable in the titanite stability field, ranging from ~ 0.8 to < 0.1 . The modeled Ti-in-quartz values show a strong increase with T, and a weak decrease with P. At T above $\sim 230^\circ\text{C}$, the positive correlation between Si-in-phengite and P, and negative correlation with T, is observed, as predicted experimentally (Massonne & Schreyer, 1987; Massonne & Szpurka, 1997). However, at low T and higher P, Si-in-phengite increases with both P and T.

Figure 7. Pseudosections representative of the SSZ metagranites. a) TS-051, a low-T mylonitic granite with high Si, moderate Fe, low Ca, low Na, and high K; and b) TS-054, a moderate-T mylonitic granite with lower Fe, higher Ca and Na, and lower K. The stability fields of phengite and the Ti-rich phases titanite, rutile, and ilmenite are shown. Stars indicate the deformation P-T conditions calculated from Ti-in-quartz and Si-in-phengite (see text for explanation), with the shaded areas representing the error. Gold = latest deformation, orange = relict, red = oldest relict.



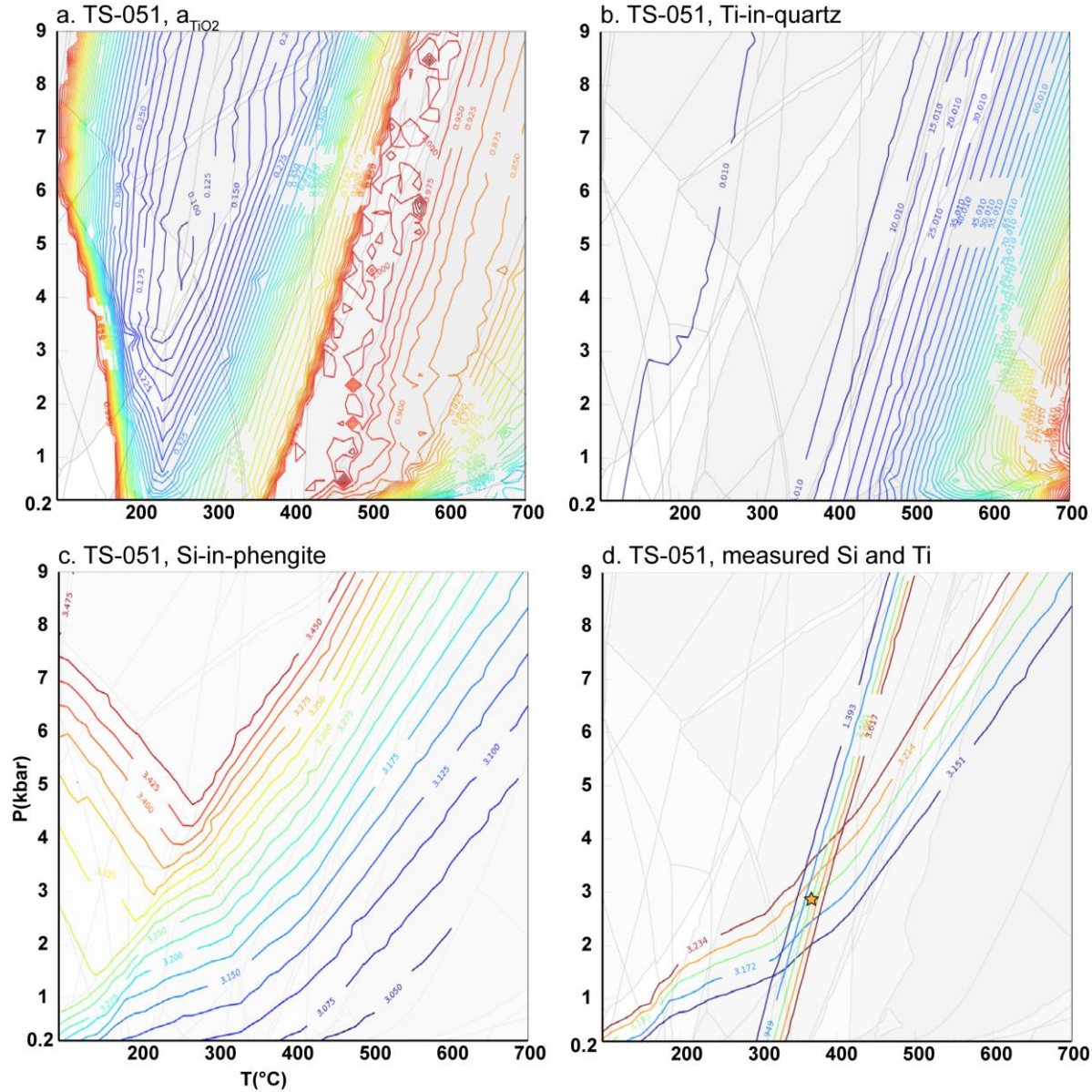


Figure 8. a) Isopleths of a_{TiO_2} , modeled using the bulk rock composition. b) Isopleths of Ti-in-quartz (ppm), calculated from the modeled a_{TiO_2} , P, and T according to Thomas et al. (2010). c) Isopleths of Si-in-phengite (pfu) extracted from the Pheng(HP) activity model. d) The intersection of Ti- and Si- isopleths that correspond to the Ti- and Si- contents measured in quartz and phengite respectively, yielding a single P-T (gold star). Isopleths are shown for the measured Ti and Si values (green) ± 2 standard deviations, with warmer colors for higher values.

4.5 P-T of Deformation

The intersection of the modelled Si- and Ti- isopleths that match the measured Si- and Ti- in phengite and quartz respectively yields a single P-T condition for each sample (Fig. 8d). These results are summarized in Table 1 and Figure 9. Maximum- and minimum P and T conditions for each sample are calculated using the measured Si- and Ti- contents ± 2 standard deviations. This reflects the natural variation within each quartz- and phengite population, which is larger than

the analytical error. The estimated P-T conditions range from $300^{+44.0}_{-68.5}$ °C at $0.74^{+1.0}_{-0.74}$ kbar in a late, mm-scale shear band, and $303^{+21.6}_{-23.9}$ °C at $1.51^{+0.69}_{-0.69}$ kbar in mylonites proximal to the brittle fault, to $444.0^{+33.0}_{-37.3}$ °C at $4.66^{+1.33}_{-1.25}$ kbar in mylonites far into the footwall, and $490.2^{+12.0}_{-13.9}$ °C at $6.73^{+0.57}_{-0.65}$ kbar preserved in relict assemblages within moderately proximal mylonites. Two outliers are not considered ($326.9^{+46.9}_{-80.0}$ °C at $0.13^{+1.61}_{-0.13}$ kbar and $442.6^{+24.2}_{-57.2}$ °C at $7.58^{+3.42}_{-4.01}$ kbar), due to anomalously large errors. Note that the accuracy of the absolute values is dependent on the various parameters used in the petrologic modeling and the Ti-in-quartz thermobarometer calibration, for which an error estimate of ± 25 °C or ± 1.2 kbar is considered reasonable (Thomas et al., 2010). Because the same model inputs and calibration were used for all samples, the P-T estimates are considered highly precise, and relative differences between samples are therefore reliable.

The modelled mineral assemblages at the estimated P-T conditions of equilibration match the observed assemblages well, typically comprising quartz, Na-rich plagioclase, phengite, biotite, and epidote, with minor to trace titanite, and K-feldspar in some samples. The a_{TiO_2} at the P-T of equilibration ranges from 0.28 to 1.00, with most values falling in the range 0.3-0.5.

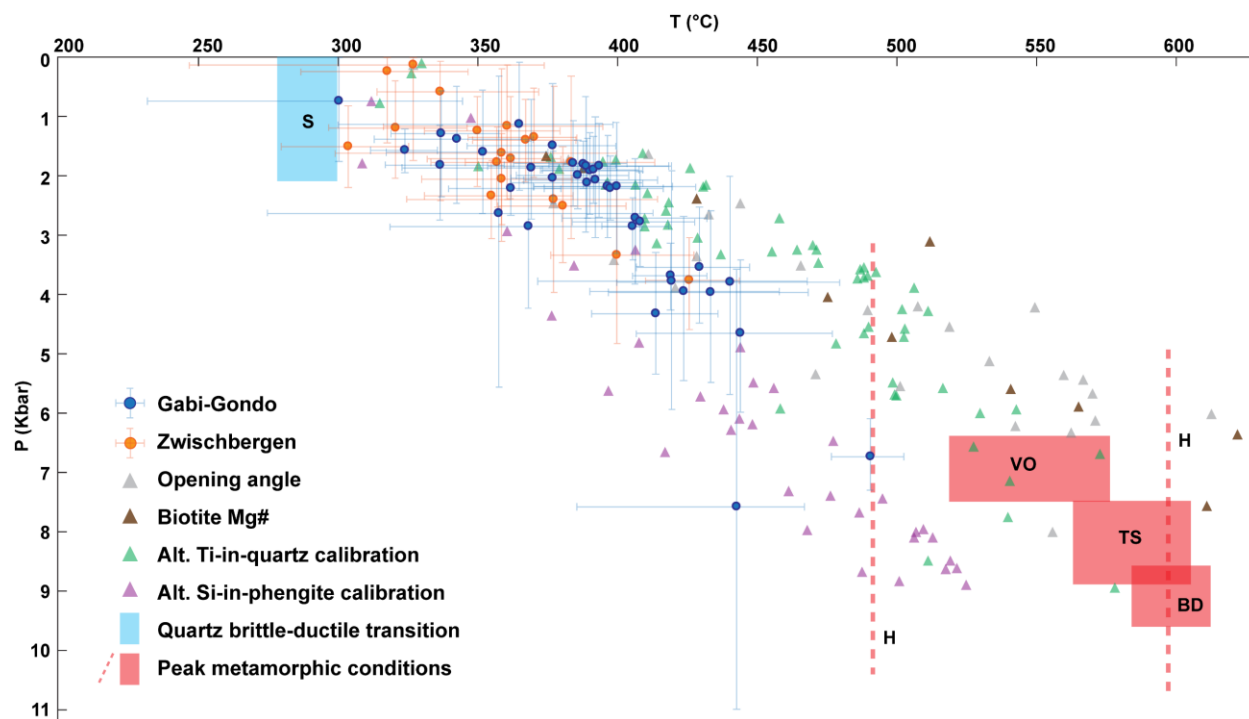


Figure 9. Deformation P-T conditions of samples from the SSZ, estimated using the Ti-in-quartz equation of Thomas et al. (2010) and Si-in-phengite from the solution model of Powell and Holland (1999). Also shown are P-T estimates for all samples made using alternative methods (see text for details). Independent estimates of peak metamorphic conditions provide an upper P-T limit on possible deformation conditions, while the onset of brittle deformation in quartz provides a lower limit. Peak P-T: BD = Baxter and DePaolo (2000), H = Haertel et al. (2013), TS = this study, and VO = Vance and O’Nions (1992). Brittle-ductile transition in quartz: S = Stipp et al. (2002).

4.6 Effective Bulk Composition

Note that our approach assumes that the entire bulk composition is available during deformation and re-equilibration of quartz and phengite. However, some components, such as Na and Si, may remain sequestered in relict grains and porphyroclasts (such as large albite grains or relict high-Si phengite), removing them from the effective bulk composition. To evaluate the potential effects of this on our P-T estimates, we re-calculated the P-T for sample TS-054 (abundant coarse-grained feldspar, relict high-Si and younger lower-Si phengite, Fig. 6), using a bulk composition from which we had removed the equivalent of 3 weight% high-Si phengite $\text{K}(\text{Al}_{1.5}\text{Mg}_{0.5})(\text{Al}_{0.73}\text{Si}_{3.27}\text{O}_{10})(\text{OH})$ and 15 weight% albite $\text{NaAlSi}_3\text{O}_8$. This yielded P-T conditions of $402.4^{+28.0}_{-28.1} \text{ } ^\circ\text{C}$ at $2.52^{+0.96}_{-0.90} \text{ kbar}$ for the most recently-equilibrated quartz-phengite pair, which is well within error of our original estimate ($396.5^{+23.0}_{-26.9} \text{ } ^\circ\text{C}$ at $2.18^{+0.86}_{-0.86} \text{ kbar}$). The impact of relict phases altering the effective bulk composition on our P-T estimates is thus considered negligible.

4.7 Alternative Thermobarometers and Calibrations

We investigated several alternative thermobarometers, as summarized in Figure 9.

4.7.1 Quartz C-axis Opening Angles

For dynamically recrystallized quartz, the angle between the “limbs” on a C-axis pole figure is strongly temperature dependent (Faleiros et al., 2016; Law, 2014), although a lesser pressure dependence has also been suggested (Faleiros et al., 2016). We use the empirically-derived thermobarometer equation of Faleiros et al. (2016), intersected with our modeled and measured Si-in-phengite, to estimate the P-T of deformation.

Crystallographic orientation measurements were obtained for domains of dynamically recrystallized quartz by electron backscatter diffraction (EBSD), using a JEOL-7001F scanning electron microscope operated at low vacuum, equipped with a Hikari EBSD detector and EDAX OIM software, at the University of Southern California Core Center of Excellence in Nano Imaging. Probe-polished samples were further polished in colloidal silica, and analyzed at 20-25 kV accelerating voltage, 15 mm working distance, 70° specimen tilt, and a step size of 0.75-8 μm . Angles were measured on c-axis pole figures following Law (2014) and Faleiros et al. (2016). Data are available in Cawood and Platt (2020d). Dynamically recrystallized grain sizes and their interpretation will be presented in a later publication.

4.7.2 Biotite Composition

We investigated the P-T conditions indicated by the intersection of our modeled and measured Si-in-phengite with our modeled and measured biotite Mg number ($\text{Mg}/(\text{Fe}+\text{Mg})$).

Biotite composition was analyzed by microprobe together with that of phengite, as detailed above.

4.7.3 Alternative Ti-in-Quartz Calibration

Here we calculate P-T in the same way as described above, but use the Ti-in-quartz thermobarometer calibration of Huang and Audetat (2012). Note that this expression does not take a_{TiO_2} into account.

4.7.4 Alternative Si-in-Phengite Equation

The previous approaches have all relied on the same Pheng(HP) solution model. As an alternative, we estimate deformation P-T using the equation of Caddick and Thompson (2008), intersected with our modeled and measured Ti-in-quartz values. Their equation is based on the Coggon and Holland (2002) phengite solution model, but was developed for metapelites.

4.8 Age of Deformation

The metagranites of the SSZ footwall lack phases suitable for petrochronology, such as notable monazite or deformed titanite. We therefore use the location and estimated deformation temperature of each sample to link it to existing thermochronological data.

Thermochronological data for the central portion of the SSZ footwall is presented in Figure 10. Different mineral thermochronological systems reflect cooling through different temperatures. All points from the same system (reflecting the same temperature) are linked by a curve; these curves represent approximate isothermal lines, showing when the currently-exposed rocks of the footwall were at the same temperature. To estimate the timing of deformation of a sample, its distance from the brittle fault is plotted on the x-axis. To determine its y-co-ordinate, the x-co-ordinate is traced vertically upwards until it intersects the isothermal curve representing the temperature we have estimated for that sample's deformation. The corresponding age for this point is then read off the y-axis. If a sample was deformed at a temperature not exactly matched by the cooling temperature of one of the thermochronometer systems, its y-co-ordinate was estimated based on the thermochronometers with the most similar temperatures. This approach suggests that our highest-P-T samples preserve deformation from ~24.5 Ma, whereas a lower P-T sample was overprinted at ~11.3 Ma. Error in these age estimates stems from error in the compiled thermochronological data (average 2 standard deviation of ± 2 Ma), sample locations (assigned ± 20 m), and our T estimates (average 2 standard deviation of $^{+25.2}_{-30.4}$ °C).

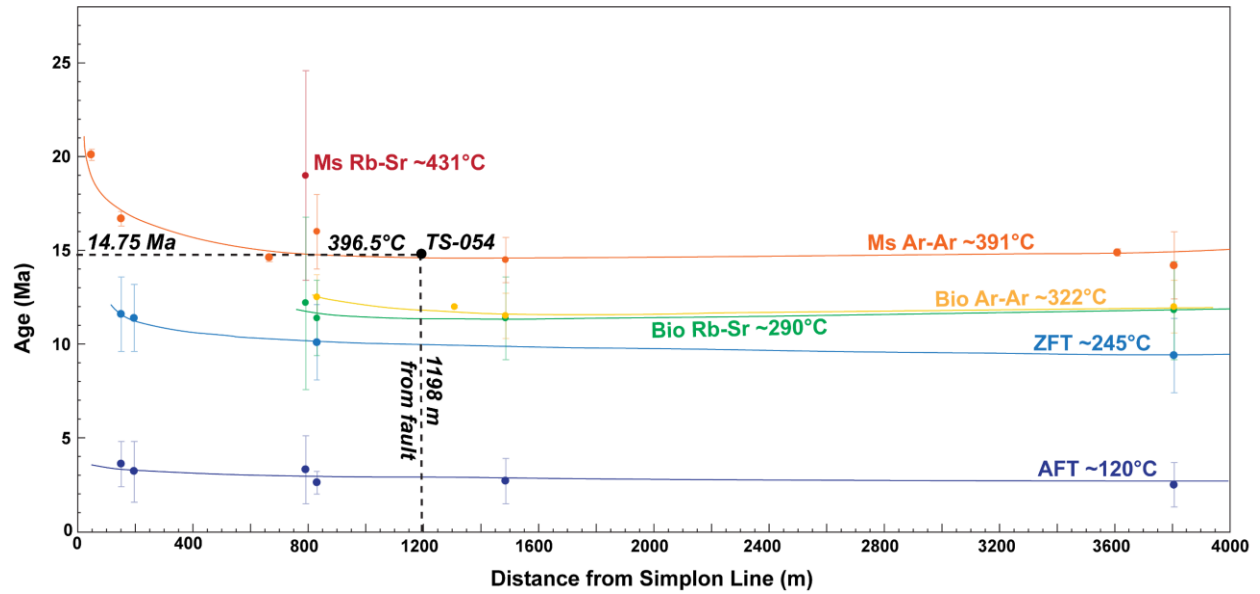


Figure 10. Thermochronology of the SSZ footwall, plotted as cooling ages against distance from the brittle Simplon Line. Curves linking each mineral system are labelled with that system's approximate cooling temperature. The location of sample TS-054 and the temperature of its youngest pervasive deformation are overlain on the plot, to illustrate how these values are used to read off the approximate time when TS-054 experienced that temperature. Thermochronology data were compiled by Campani et al. (2010b), from Baxter et al. (2002), Campani et al. (2010a), Hetherington and Villa (2007), Hunziker and Bearth (1969), Jager et al. (1967), Purdy and Jager (1976), Soom (1990), and Wagner et al. (1977). Ms = muscovite, Bio = biotite, ZFT = zircon fission track, AFT = apatite fission track.

4.9 P-T-t Paths

Most samples display incomplete overprinting by subsequent deformation, and in some, relict quartz-phengite pairs can be reliably distinguished from quartz-phengite pairs related to later, overprinting deformation. For these samples, the P-T conditions of both the earlier and subsequent deformation were estimated, yielding two or three points on a P-T path (Fig. 11). All of our P-T paths are approximately parallel. Compared to the path modelled by Campani et al. (2010b), our paths are significantly steeper, possibly reflecting exhumation outpacing cooling.

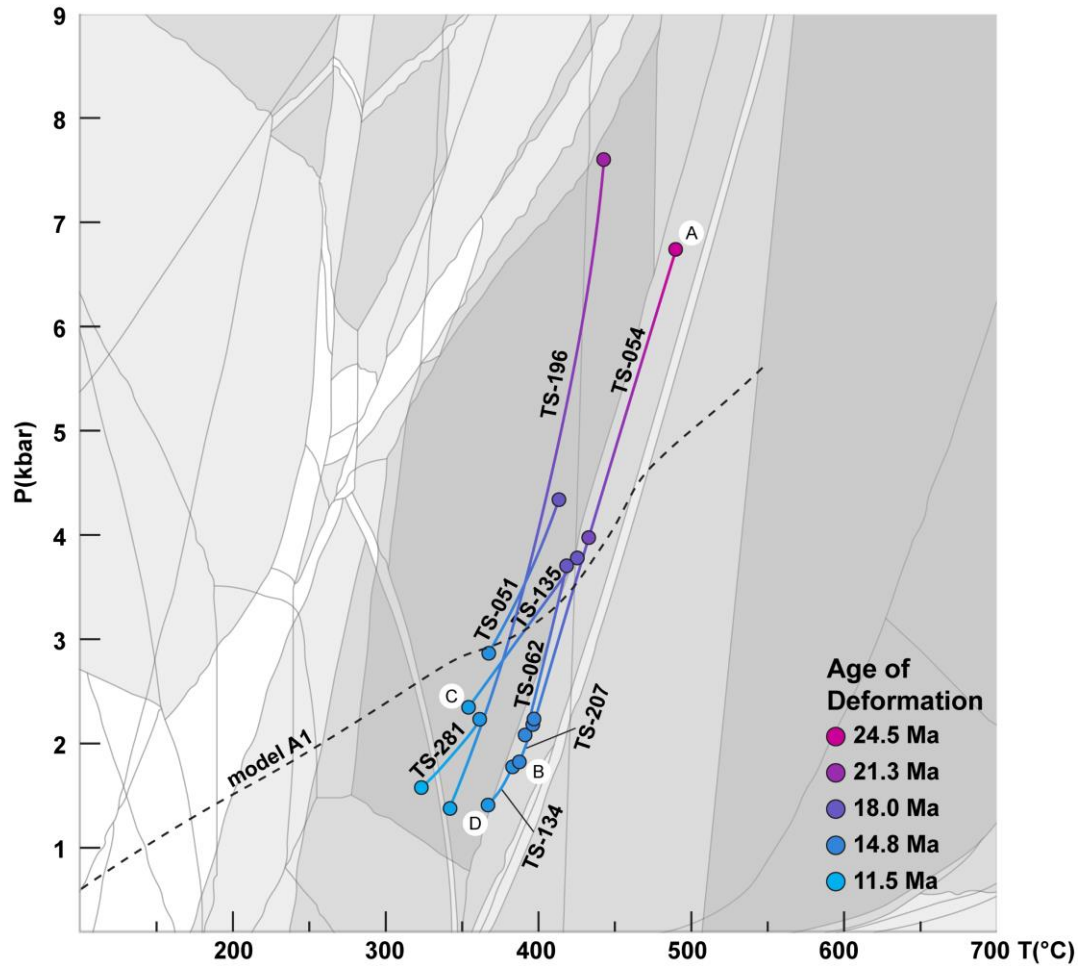


Figure 11. P-T paths derived from samples with both relict- and younger quartz-phengite pairs, overlain on a representative pseudosection (TS-054), and color coded by age. The black stippled line is a P-T path modeled by Campani et al. (2010b, their model A1), based on thermochronological data. A-B represents different conditions experienced by the same rock at different times (temporal variations in P-T, due to exhumation), whereas B-C-D represent deformation at different conditions experienced by different parts of the SSZ footwall at approximately the same time (spatial variation in P-T).

4.10 Peak Metamorphic Conditions

To provide an additional constraint on the maximum possible P-T conditions of deformation, multi-equilibrium thermobarometry was used to estimate the peak metamorphic conditions in the SSZ footwall, using Thermocalc version 3.33 (Powell & Holland, 1988, updated 2009) and following the “average P-T” approach of Powell and Holland (1994). We investigated sample TS-026 from the northern region of the SSZ footwall, a metapelite cut by narrow, diffuse amphibole-bearing bands. The metapelitic parts have the peak metamorphic assemblage quartz-garnet-plagioclase-staurolite-biotite-ilmenite-rutile-calcite-kyanite, with minor retrograde chlorite and muscovite.

The compositions of biotite, garnet, ilmenite, feldspar, and staurolite were measured on a JEOL JXA-8200 microprobe at the University of California Los Angeles, using a 5 μm spot size,

15 KV accelerating voltage, 10 nA current, and a counting time of 20 seconds on-peak and 10 seconds background on either side. Data are available in Cawood and Platt (2020e). Using $X_{\text{H}_2\text{O}}$ (proportion of H_2O to CO_2) of 0.6 (after Vance & O’Nions, 1992), we calculate peak metamorphic conditions of $584 \pm 21^\circ\text{C}$ at 8.2 ± 0.7 kbar, which compares well with previous estimates (Fig. 9).

5 Discussion

5.1 Do These P-T-t Values Represent Deformation Conditions?

We observe lower Ti in both SGR- and BLG/SGR- recrystallized quartz, compared to relict coarser quartz grains and ribbons (Fig. 6). This supports previous findings that GBM, SGR, and BLG are all able to at least partially reset quartz Ti contents (Ashley et al., 2014; Nachlas & Hirth, 2015; Nachlas et al., 2014, 2018;), and is in contrast to the conclusions of Grujic et al. (2011), that Ti content is only modified by GBM, and of Haertel et al. (2013), that Ti content is only modified by GBM and BLG. Similarly, in most samples with both older, coarse-grained phengite laths and younger clusters or rims of fine-grained, synkinematic phengite, the younger phengite has lower Si contents. This is consistent with the findings of previous studies, that have used multiple generations of phengite to elucidate P-T conditions over time (e.g. Massonne, 2015; Santamaría-López et al., 2019). Our P-T-t estimates therefore reflect deformation conditions.

5.2 Are These P-T-t Conditions Accurate?

5.2.1 Our Data versus Independent Constraints on Deformation P-T-t

Our maximum reliable P-T value ($490.2^{+12.0}_{-13.9}^\circ\text{C}$ at $6.73^{+0.57}_{-0.65}$ kbar) is consistent with deformation during retrograde conditions, subsequent to peak metamorphism at ~ 491 – 612°C and ~ 6.4 – 9.6 kbar (Fig. 9, based on multi-equilibrium thermobarometry and Raman spectroscopy, from this study; Baxter & DePaolo, 2000; Haertel et al., 2013; Vance & O’Nions, 1992). Our minimum reliable T ($300^{+44.0}_{-68.5}^\circ\text{C}$) is consistent with the transition from viscous- to brittle behavior in quartz occurring at ~ 280 – 300°C (Stipp et al., 2002; Stöckert et al., 1999). In contrast, the deformation P of our shallowest samples ($0.24^{+1.2}_{-0.24}$ to $0.74^{+1.0}_{-0.74}$ kbar, equivalent to depths of ~ 1 – 2.8 km) is significantly lower than typical estimates for the depth of the brittle-ductile transition. Ductile mylonitization at shallow depths is however possible in areas with steep geothermal gradients, such as in regions of active extension. For example, temperatures of ~ 300 – 350°C have been estimated to occur at only ~ 1.31 kbar in the Walker Lane region of the Western United States (Zuza & Cao, 2020), and even steeper gradients have been measured in modern geothermal fields ($\sim 450^\circ\text{C}$ at ~ 1.6 – 0.8 kbar in the Larderello geothermal field, Bellani et al. 2004).

Our estimates for the timing of shearing are also consistent with independent constraints: our oldest relict deformation is indirectly dated at ~ 24.5 Ma, consistent with deformation following ~ 33 – 25 Ma peak metamorphism (Vance & O’Nions, 1992). Several studies have dated brittle fracturing, vein filling, and gouge formation in the SSZ footwall to ~ 16.5 – 5.7 Ma, based on the ages of hydrothermal monazite in fissures, vein-hosted muscovite, and gouge illite (Bergemann et al., 2020; Hetherington & Villa, 2007; Pettke et al., 1999; Zwingmann & Mancktelow, 2004). However, the transition from viscous to frictional deformation in the exposed footwall was likely diachronous from north to south. In the central part of the SSZ, the

oldest evidence for brittle faulting is 11.6 ± 1 Ma muscovite in gold-bearing quartz veins (Pettke et al., 1999), consistent with our estimates for the most recent mylonitization occurring at ~ 11.3 Ma. Importantly, the ages discussed here were not part of the thermochronology compilation used to deduce our ages.

We therefore consider our estimates to be reasonably accurate, as they are well matched by independent constraints. However, the deformation temperatures of our samples may alternatively be up to ~ 30 – 90°C too low, if the actual peak metamorphic temperatures are closer to the estimate made in this study ($\sim 584^\circ\text{C}$), rather than the lowest of the previous estimates ($\sim 491^\circ\text{C}$, based on Raman spectroscopy of vein-hosted graphite, Haertel et al., 2013).

5.2.2 Our Data versus Alternate Methods for Estimating P-T

Compared to P-T estimates based on alternate methods and calibrations, our values are similar or lower (Fig. 9). Several factors may have affected our estimates, including contamination of spot analyses; a too-large beam size that failed to resolve fine grains from Ti-bearing phases along grain boundaries; failure of the analyzed portions of phengite or quartz grains to have fully re-equilibrated during deformation; incorrectly identifying coeval, syn-kinematic phengite and quartz; incorrect assumptions regarding a_{TiO_2} ; or issues with the phengite activity model or the Ti-in-quartz calibration. However, care was taken to avoid contamination and exclude contaminated data; although analytical spots in fine-grained quartz covered several grains, the occurrence of Ti-bearing phases along grain boundaries would result in higher-than-expected Ti, rather than the lower-than-expected values we found; failure of originally high-T phengite and quartz to fully re-equilibrate would similarly yield higher-than-expected values; and careful petrography strongly supports our interpretations of which phengite-quartz pairs represent coeval deformation. Therefore, either our estimated conditions are ~ 30 – 90°C too low, due to incorrect a_{TiO_2} assumptions or issues with the phengite activity model and Ti-in-quartz calibration, or our estimates are correct. The applied method is very precise, so the relative differences in P-T conditions between samples are likely reliable.

5.3 Spatial and Temporal Variations in Deformation P-T-t in Crustal-Scale Shear Zones

Our results show that the SSZ footwall preserves evidence for retrograde deformation during exhumation, from just below amphibolite-facies conditions (490.2°C , 6.73 kbar at ~ 24.5 Ma) to lower greenschist-facies conditions (300.3°C , 0.74 kbar at ~ 11.9 Ma in a narrow shear band, and 303.7°C , 1.51 kbar at ~ 11.3 Ma in mylonites closer to the fault). Exhumation was accommodated by a kilometer-scale ductile shear zone, in which progressive localization with decreasing P-T allowed the preservation of older, relict textures further into the footwall, as subsequent deformation at lower grades overprinted an increasingly narrow zone (Fig. 12). This phenomenon has been well documented in both normal- and thrust-sense shear zones that experienced exhumation during deformation (e.g. Behr & Platt, 2011; Cooper et al., 2017; Haertel, 2012; Handy et al., 2007; Lusk & Platt, 2016, in press).

However, it is important to note that the deformation conditions preserved in rocks now exposed at surface were not experienced simultaneously: material further into the footwall has experienced a greater amount of total exhumation, and preserves deformation that occurred at higher P-T and longer ago, whereas material closer to the brittle fault has experienced less total exhumation, and has undergone overprinting over a wider range of P-T conditions, with the final preserved stage of mylonitization occurring at lower T, shallower depths, and more recently.

This is typical of crustal-scale shear zones, which display both a) evolution of P-T conditions experienced by any specific volume of rock, as activity on the shear zone advects it up- or downwards, and b) simultaneous deformation over a wide range of P-T conditions, from the high P-T of the lower crust or lithospheric mantle, to the low P-T of the upper crust. The former is less important in predominantly strike-slip faults, where little vertical motion occurs, but even strike-slip dominated faults may have some component of dip-slip, causing material advection and thus a change in P-T conditions of deformation. In the SSZ, a) is reflected by points A and B in Figures 11 and 12, with sample TS-054 experiencing significantly different P-T conditions at different times, as it underwent exhumation and cooling. In contrast, b) is illustrated by points B, C, and D, which represent different samples that were deformed at different conditions at approximately the same time, due to their different positions within the SSZ footwall.

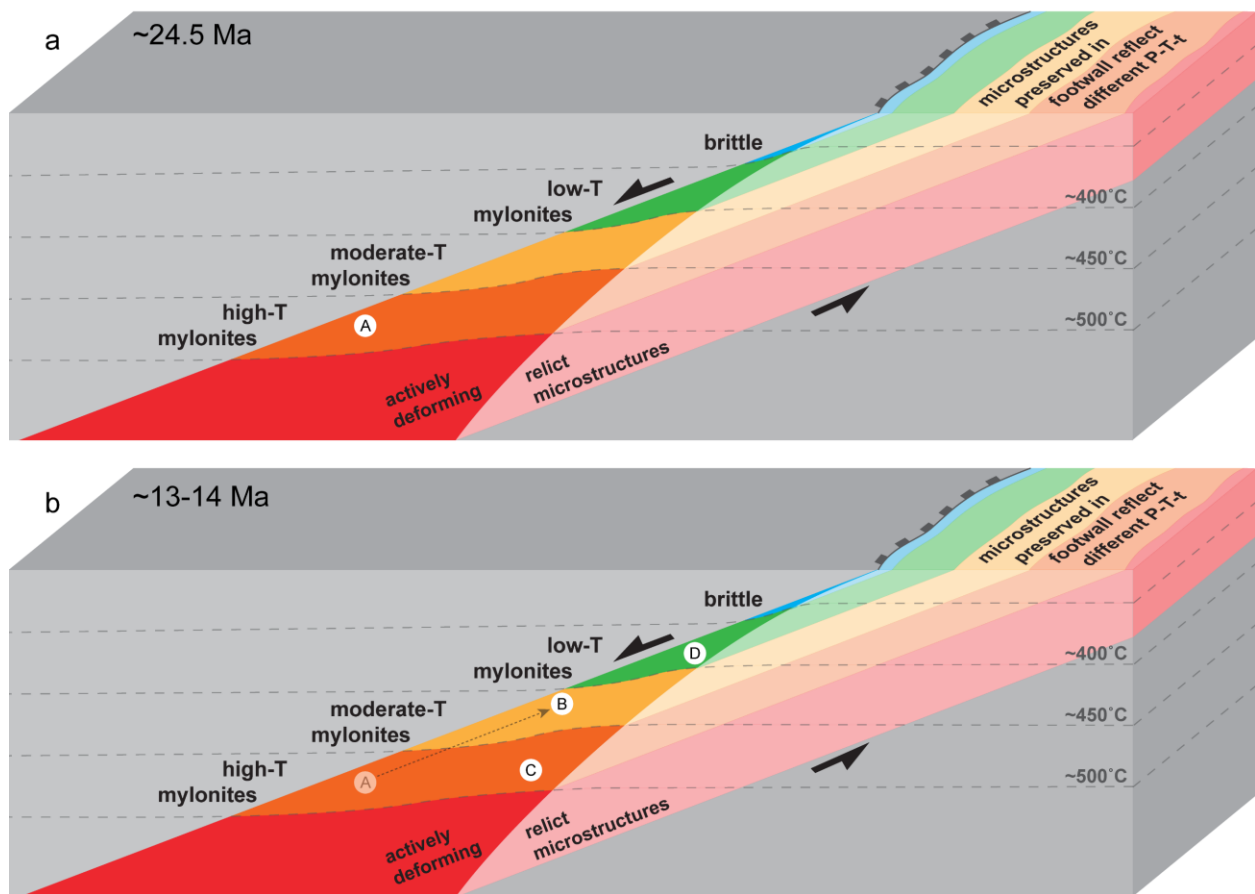


Figure 12. A cartoon illustrating how the P-T of deformation varies both temporally (from A to B) and spatially (B, C, and D) in an exhuming shear zone such as the SSZ. Legend is the same as in Figure 2. Adapted from Haertel (2012) and Handy et al. (2007).

6 Conclusions

By combining two mineral-chemistry thermobarometers that are reset by deformation (Si-in-phengite and Ti-in-quartz) with modeled bulk rock a_{TiO_2} and compiled thermochronology, we have determined the P-T-t of deformation for a number of metagranitic samples extending into the footwall of the normal-sense SSZ, despite a dearth of commonly-used thermobarometers (such as garnet) and petrochronometers (such as monazite). Careful microscopy allowed us to identify phases deformed and re-equilibrated simultaneously, despite a long history of structural overprinting. This work highlights both the wide range of conditions over which deformation occurs in crustal-scale shear zones, and the evolution of conditions as seen by a single sample over time. Our estimates for the range of P-T conditions during deformation are bracketed by independent constraints on peak metamorphic conditions at the upper end, and the frictional-viscous transition in quartz at the lower end. This supports our methodology and results in general. However, it does not allow us to determine whether our estimates are accurate, or up to $\sim 90^\circ\text{C}$ too low, possibly reflecting ongoing uncertainties in the Ti-in-quartz thermobarometer calibrations and estimation of a_{TiO_2} .

Acknowledgments, Samples, and Data

The authors declare no conflicts of interest. Datasets generated and used in this study are available at: Cawood and Platt (2020a,b,c,e), with license CC BY-SA 4.0, and Cawood and Platt (2020d), with license CC BY 4.0. Thermochronological data used in this study are compiled in Campani et al. (2010b). This research was supported by the US National Science Foundation (NSF) grant EAR-1650173. In addition, we acknowledge the use of the Arizona State University SIMS Facility, supported by NSF grant EAR-1819550. The authors thank Gareth Seward and Rosario Esposito for assistance with microprobe analyses, Rick Hervig and Lynda Williams with SIMS work, Claire Bucholz with XRF analyses, John Curulli and Matt Mecklenberg with EBSD, and Gareth Cawood, Karen Rudnick, and Peter Wynn for support in the field. This study benefited from helpful discussions with Alex Lusk and Will Schmidt.

References

- Ackerson, M.R., Mysen, B.O., Tailby, N.D., & Watson, E.B. (2018), Low-temperature crystallization of granites and the implications for crustal magmatism. *Letters to Nature*, 559. doi: 10.1038/s41586-018-0264-2
- Anderson, J.L. (1996), Status of thermobarometry in granitic batholiths. *Transactions of the Royal Society of Edinburgh: Earth Sciences*, 87, 125-138.
- Anderson, J.L., Barth, A.P., Wooden, J.L., & Mazdab, F. (2008), Thermometers and thermobarometers in granitic systems. *Reviews in Mineralogy and Geochemistry*, 69, 121-142. doi: 10.2138/rmg.2008.69.4
- Ashley, K.T., Carlson, W.D., Law, R.D., & Tracy, R.J. (2014), Ti resetting in quartz during dynamic recrystallization: Mechanisms and significance. *American Mineralogist*, 99, 2025-2030. doi: 10.2138/am-2014-4943

- Ashley, K.T., & Law, R.D. (2015), Modeling prograde TiO₂ activity and its significance for Ti-in-quartz thermobarometry of pelitic metamorphic rocks. *Contributions to Mineralogy and Petrology*, 169, doi: 10.1007/s00410-015-1118-7
- Ashley, K.T., Webb, L., Spear, F.S., & Thomas, J.B. (2013), P-T-D histories from quartz: A case study of the application of the TitaniQ thermobarometer to progressive fabric development in metapelites. *Geochemistry, Geophysics, Geosystems*, 14. doi: 10.1002/ggge.20237
- Baxter, E.F., & DePaolo, D.J. (2000), Field measurements of slow metamorphic rates at temperatures of 500° to 600°C. *Science*, 288, 1411-1414. doi: 10.1126/science.288.5470.1411
- Baxter, E.F., DePaolo, D.J., & Renne, P.R. (2002). Spatially correlated anomalous ⁴⁰Ar/³⁹Ar “age” variations in biotites about a lithologic contact near Simplon Pass, Switzerland: A mechanistic explanation for excess Ar. *Geochimica et Cosmochimica*, 66, 1067-1083. doi: 10.1016/S0016-7037(01)00828-6
- Behr, W. M., & Platt, J. P. (2011), A naturally constrained stress profile through the middle crust in an extensional terrane. *Earth and Planetary Science Letters*, 303, 181-192. doi: 10.1016/j.epsl.2010.11.044
- Bellani, S., Brogi, A., Lazzarotto, A., Liotta, D., & Ranalli, G. (2004), Heat flow, deep temperatures and extensional structures in the Larderello Geothermal Field (Italy): constraints on geothermal fluid flow. *Journal of Volcanology and Geothermal Research*, 132, 15-29. doi: 10.1016/S0377-0273(03)00418-9
- Bergemann, C.A., Gnos, E., Berger, A., Janots, E., & Whitehouse, M.J. (2020), Dating tectonic activity in the Lepontine dome and Rhone-Simplon Fault regions through hydrothermal monazite-(Ce). *Solid Earth*, 11, 199-222. doi: 10.5194/se-11-199-2020
- Bestmann, M., & Pennacchioni, G. (2015), Ti distribution in quartz across a heterogeneous shear zone within a granodiorite: The effect of deformation mechanism and strain on Ti resetting. *Lithos*, 227, 37-56. doi: 10.1016/j.lithos.2015.03.009
- Caddick, M.J., & Thompson, A.B. (2008), Quantifying the tectono-metamorphic evolution of pelitic rocks from a wide range of tectonic settings: Mineral compositions in equilibrium. *Contributions to Mineralogy and Petrology*, 156, 177-195. doi: 10.1007/s00410-008-0280-6
- Campani, M., Herman, F., & Mancktelow, N. (2010b). Two- and three-dimensional thermal modeling of a low-angle detachment: Exhumation history of the Simplon Fault Zone, central Alps. *Journal of Geophysical Research*, 115. doi: 10.1029/2009JB007036
- Campani, M., Mancktelow, N., & Courrioux, G. (2014), The 3D interplay between folding and faulting in a syn-orogenic extensional system: the Simplon Fault Zone in the Central Alps (Switzerland and Italy). *Swiss Journal of Geoscience*, 107, 251-271. doi: 10.1007/s00015-014-0163-y
- Campani, M., Mancktelow, N., Seward, D., Rolland, Y., Müller, W., & Guerra, I. (2010a), Geochronological evidence for continuous exhumation through the ductile-brittle transition

- 872 along a crustal-scale low-angle normal fault: Simplon Fault Zone, central Alps. *Tectonics*, 29.
873 doi: 10.1029/2009TC002582
- 874 Cavalcante, C., Lagoeiro, L., Fossen, H., Egydio-Silva, M., Morales, L.F.G., Ferreira, F., &
875 Conte, T. (2018), Temperature constraints on microfabric patterns in quartzofeldspathic
876 mylonites, Ribeira belt (SE Brazil). *Journal of Structural Geology*, 115, 243-262. doi:
877 10.1016/j.jsg.2018.07.013
- 878 Cawood, T., & Platt, J.P. (2020a), Microprobe analyses of phengite and biotite in granitic
879 mylonites from the Simplon Shear Zone, Version 1.0. Interdisciplinary Earth Data Alliance
880 (IEDA). doi: 10.26022/IEDA/111621
- 881 Cawood, T., & Platt, J.P. (2020b), Ti-in-quartz analyses of metagranitic mylonites from the
882 Simplon Shear Zone, Version 1.0. Interdisciplinary Earth Data Alliance (IEDA). doi:
883 10.260222/IEDA/111620
- 884 Cawood, T., & Platt, J.P. (2020c), Bulk rock composition of mylonitic granites from the Simplon
885 Shear Zone, Version 1.0. Interdisciplinary Earth Data Alliance (IEDA). doi:
886 10.26022/IEDA/111618
- 887 Cawood, T., & Platt, J.P. (2020d), Quartz EBSD data from the Simplon Shear Zone, central
888 Alps. Mendeley Data. doi: 10.17632/whp6ppzd98.1
- 889 Cawood, T. & Platt, J.P. (2020e), Microprobe analyses of peak metamorphic minerals in a
890 metapelite from the Simplon Shear Zone footwall, Version 1.0. Interdisciplinary Earth Data
891 Alliance (IEDA). doi: 10.26022/IEDA/111622
- 892 Chambers, J.A., & Kohn, M.J. (2012), Titanium in muscovite, biotite, and hornblende:
893 Modeling, thermometry, and rutile activities of metapelites and amphibolites. *American*
894 *Mineralogist*, 97, 543-555. doi: 10.2138/am.2012.3890
- 895 Coggon R., & Holland, T.J.B. (2002), Mixing properties of phengitic micas and revised garnet-
896 phengite thermobarometers. *Journal of Metamorphic Geology*, 20, 683-696. doi: 10.1046/j.1525-
897 1314.2002.00395.x
- 898 Connolly, J.A.D. (2005), Computation of phase equilibria by linear programming: A tool for
899 geodynamic modeling and its application to subduction zone decarbonation. *Earth and Planetary*
900 *Science Letters*, 236, 524-541. doi: 10.1016/j.epsl.2005.04.033
- 901 Cooper, F.J., Platt, J.P., & Behr, W.M. (2017), Rheological transitions in the middle crust:
902 insights from Cordilleran metamorphic core complexes. *Solid Earth*, 8, 199-215. doi:
903 10.5194/se-8-199-2017
- 904 Cox S.F. (2006), Coupling between deformation, fluid pressures, and fluid flow in ore-producing
905 hydrothermal systems at depth in the crust. *Economic Geology 100th Anniversary Volume*, 39-75.
- 906 Deer, W.A., Howie, R.A., & Zussman, J. (2013), An introduction to the rock-forming minerals,
907 3rd ed. London: Mineralogical Society.

- 908 Faleiros, F.M., Moraes, R., Pavan, M., & Campanha, G.A.C. (2016), A new empirical calibration
909 of the quartz c-axis fabric opening-angle deformation thermometer. *Tectonophysics*, 671, 173-
910 182. doi: 10.1016/j.tecto.2016.01.014
- 911 Gallagher, C., & Bromiley, G. (2013), *Ti in quartz standards*. Available:
912 [https://www.ed.ac.uk/geosciences/facilities/ionprobe/standard-materials-](https://www.ed.ac.uk/geosciences/facilities/ionprobe/standard-materials-available/tiquartzstandards)
913 [available/tiquartzstandards](https://www.ed.ac.uk/geosciences/facilities/ionprobe/standard-materials-available/tiquartzstandards)
- 914 Gerlach, H. (1869), Karte der Penninischen Alpen, 1:20,000. *Neue Denkschriften zur Schweizer*
915 *Naturgeschichte*.
- 916 Ghent, E.D., & Stout, M.Z. (1984), TiO₂ activity in metamorphosed pelitic and basic rocks:
917 Principles and applications to metamorphism in southeastern Canadian Cordillera. *Contributions*
918 *to Mineralogy and Petrology*, 86, 248-255.
- 919 Grasemann, B., & Mancktelow, N.S. (1993), Two-dimensional thermal modelling of normal
920 faulting: The Simplon Fault Zone, central Alps, Switzerland. *Tectonophysics*, 225, 155-165. doi:
921 10.1016/0040-1951(93)90277-Q
- 922 Grujic, D., Ashley, K.T., Coble, M.A., Coutand, I., Kellett, D.A., Larson, K.P., et al. (2020),
923 Deformational temperatures across the Lesser Himalayan Sequence in Eastern Bhutan and their
924 implications for the deformation history of the Main Central Thrust. *Tectonics*, 39. doi:
925 10.1029/2019TC005914
- 926 Grujic, D., Stipp, M., & Wooden, J.L. (2011), Thermometry of quartz mylonite: Importance of
927 dynamic recrystallization on Ti-in-quartz reequilibration. *Geochemistry, Geophysics,*
928 *Geosystems*, 12. doi: 10.1029/2010GC003368
- 929 Haertel, M. (2012), Strain localization in a retrograde shear zone: The Simplon Fault Zone as an
930 example, (Doctoral dissertation). Bern: Institut für Geologie, Universität Bern.
- 931 Haertel, M., & Herwegh, M. (2014), Microfabric memory of vein quartz for strain localization in
932 detachment faults: A case study of the Simplon fault zone. *Journal of Structural Geology*, 68,
933 16-32. doi: 10.1016/j.jsg.2014.08.001
- 934 Haertel, M., Herwegh, M., & Pettke, T. (2013), Titanium-in-quartz thermometry on
935 synkinematic quartz veins in a retrograde crustal-scale normal fault zone. *Tectonophysics*, 608,
936 468-481. doi: 10.1016/j.tecto.2013.08.042
- 937 Handy M.R., Hirth G., & Bürgmann R. (2007), Continental fault structure and rheology from the
938 frictional-to-viscous transition downwards. In M. Handy, G. Hirth, N. Hovius (Eds), *Tectonic*
939 *faults: agents of change on a dynamic Earth*. Cambridge MA: The MIT Press.
- 940 Hetherington, C.J., & Villa, I.M. (2007), Barium silicates of the Berisal Complex, Switzerland:
941 A study in geochronology and rare-gas release systematics. *Geochimica et Cosmochimica Acta*,
942 71, 3336-3347. doi: 10.1016/j.gca.2007.05.001

- 943 Holland, T.J.B., Baker, T., & Powell, R. (1998), Mixing properties and activity-composition
944 relationships of chlorites in the system MgO-FeO-Al₂O₃-SiO₂-H₂O. *European Journal of*
945 *Mineralogy*, 10, 395-406.
- 946 Holland, T., & Powell, R. (1991), A compensated-Redlich-Kwong (CORK) equation for
947 volumes and fugacities of CO₂ and H₂O in the range 1 bar to 50 kbar and 100-1600°C.
948 *Contributions to Mineralogy and Petrology*, 109, 265-273.
- 949 Holland, T.J.B., & Powell, R. (1998), An internally-consistent thermodynamic dataset for phases
950 of petrological interest. *Journal of Metamorphic Geology*, 16, 309-343. doi: 10.1111/j.1525-
951 1314.1998.00140.x
- 952 Huang, R., & Audetat, A. (2012), The titanium-in-quartz (TitaniQ) thermobarometer: A critical
953 examination and re-calibration. *Geochimica et Cosmochimica Acta*, 84, 75-89. doi:
954 10.1016/j.gca.2012.01.009
- 955 Huntington, K. W., & K. A. Klepeis. (2018), Challenges and opportunities for research in
956 tectonics: Understanding deformation and the processes that link Earth systems, from geologic
957 time to human time: A community vision document submitted to the US National Science
958 Foundation. Available: <http://hdl.handle.net/1773/40754>
- 959 Hunziker, J.C., & Bearth, P. (1969), Rb-Sr Altersbestimmungen aus den Walliser-Alpen:
960 Biotitalterswerte und ihre Bedeutung für die Abkühlungsgeschichte der alpinen Metamorphose.
961 *Eclogae Geologicae Helveticae*, 62, 205-222.
- 962 Jäger, E., Niggli, E., & Wenk, E. (1967), Rb-Sr Altersbestimmungen an Glimmern der
963 Zentralpen. *Beiträge zur Geologischen Karte der Schweiz*, 134.
- 964 Kohn, M.J., & Northrup, C.J. (2009), Taking mylonites' temperatures. *Geology*, 37, 47-50, doi:
965 10.1130/G25081A.1
- 966 Law, R.D. (2014), Deformation thermometry based on quartz c-axis fabrics and recrystallization
967 microstructures: A review. *Journal of Structural Geology*, 66, 129-161. doi:
968 10.1016/j.jsg.2014.05.023
- 969 Lusk, A.D., & Platt, J.P. (2016), *Temperature-stress profile across an exhumed Caledonian*
970 *shear zone, NW Scotland*. Paper presented at the American Geophysical Union Fall Meeting, San
971 Francisco, CA. Bibcode: 2016AGUFM.T21D2867L
- 972 Lusk, A.D., & Platt, J.P. The deep structure and rheology of a plate-boundary shear zone:
973 Constraints from an exhumed Caledonian shear zone, NW Scotland. *Lithosphere*, in press. doi:
974 10.2113/2020/8824736
- 975 Mancel, P., & Merle, O. (1987), Kinematics of the northern part of the Simplon line (Central
976 Alps). *Tectonophysics*, 135, 265-275.
- 977 Mancktelow, N. (1985), The Simplon Line: A major displacement zone in the western Lepontine
978 Alps. *Eclogae Geologicae Helveticae*, 78, 73-96.

- 979 Mancktelow, N.S. (1987), Quartz textures from the Simplon Fault Zone, southwest Switzerland
980 and north Italy. *Tectonophysics*, 135, 133-153.
- 981 Mancktelow, N.S., & Pennacchioni, G. (2004), The influence of grain boundary fluids on the
982 microstructure of quartz-feldspar mylonites. *Journal of Structural Geology*, 26, 47-69. doi:
983 10.1016/S0191-8141(03)00081-6
- 984 Massonne, H-J. (2010), Phase relations and dehydration behavior of calcareous sediments at
985 very-low to low grade metamorphic conditions. *Periodico di Mineralogia*, 79, 21-43.
- 986 Massonne, H-J. (2015), Derivation of P-T paths from high-pressure metagranites – Examples
987 from the Gran Paradiso Massif, western Alps. *Lithos*, 226, 265-279. doi:
988 10.1016/j.lithos.2014.12.024
- 989 Massonne, H-J., Cruciani, G., Franceschelli, M., & Musumeci, G. (2017), Anticlockwise
990 pressure-temperature paths record Variscan upper-plate exhumation: Example from micaschists
991 of the Porto Vecchio region, Corsica. *Journal of Metamorphic Geology*, 36, 55-77. doi:
992 10.1111/jmg.12283
- 993 Massonne, H-J., & Schreyer, W. (1987), Phengite geobarometry based on the limiting
994 assemblage with K-feldspar, phlogopite, and quartz. *Contributions to Mineralogy and Petrology*,
995 96, 212-224.
- 996 Massonne, H-J., & Szpurka, Z. (1997), Thermodynamic properties of white micas on the basis of
997 high-pressure experiments in the systems K_2O - MgO - Al_2O_3 - SiO_2 - H_2O and K_2O - FeO - Al_2O_3 -
998 SiO_2 - H_2O . *Lithos*, 41, 229-250.
- 999 Menegon, L., Nasipuri, P., Stünitz, H., Behrens, H., & Ravna, E. (2011), Dry and strong quartz
1000 during deformation of the lower crust in the presence of melt. *Journal of Geophysical Research*,
1001 116. doi: 10.1029/2011JB008371
- 1002 Nachlas, W.O., & Hirth, G. (2015), Experimental constraints on the role of dynamic
1003 recrystallization on resetting the Ti-in-quartz thermobarometer. *Journal of Geophysical*
1004 *Research: Solid Earth*, 120. doi: 10.1002/2015JB012274
- 1005 Nachlas, W.O., Thomas, J.B., & Hirth, G. (2018), TitaniQ deformed: Experimental deformation
1006 of out-of-equilibrium quartz porphyroclasts. *Journal of Structural Geology*, 116, 207-222. doi:
1007 doi.org/10.1016/j.jsg.2018.07.012
- 1008 Nachlas, W.O., Whitney, D.L., Teyssier, C., Bagley, B., & Mulch, A. (2014), Titanium
1009 concentrations in quartz as a record of multiple deformation mechanisms in an extensional shear
1010 zone. *Geochemistry, Geophysics, Geosystems*, 15, 1374-1397. doi: 10.1002/2013GC005200
- 1011 Negrini, M., Stünitz, H., Berger, A., & Morales, L.F.G. (2014), The effect of deformation on the
1012 TitaniQ geothermobarometer: An experimental study. *Contributions to Mineralogy and*
1013 *Petrology*, 167. doi: 10.1007/s00410-014-0982-x
- 1014 Newton, R.C., Charlu, T.V., & Kleppa, O.J. (1980), Thermochemistry of the high structural state
1015 plagioclase. *Geochimica et Cosmochimica Acta*, 44, 933-941.

- Oriolo, S., Wemmer, K., Oyhançabal, P., Fossen, H., Schulz, B., & Siegesmund, S. (2018), Geochronology of shear zones – A review. *Earth-Science Reviews*, 185, 665-683. doi: 10.1016/j.earscirev.2018.07.007
- Pettke, T., Diamond, L.W., & Villa, I.M. (1999), Mesothermal gold veins and metamorphic devolatilization in the northwestern Alps: The temporal link. *Geology*, 27(7), 641-644. doi: 10.1130/0091-7613(1999)027<0641:MGVAMD>2.3.CO;2
- Powell, R., & Holland, T. (1988), An internally consistent dataset with uncertainties and correlations: 3. Applications to geobarometry, worked examples and a computer program. *Journal of Metamorphic Geology*, 6, 173-204.
- Powell, R., & Holland, T. (1994), Optimal geothermometry and geobarometry. *American Mineralogist*, 79, 120-133.
- Powell, R., & Holland, T. (1999), Relating formulations of the thermodynamics of mineral solid solutions: Activity modeling of pyroxenes, amphiboles, and micas. *American Mineralogist*, 84, 1-14. doi: 10.2138/am-1999-1-201
- Purdy, J.W., & Jäger, E. (1976), K-Ar ages on rock-forming minerals from the central Alps. *Memoirs of the Institute of Geology and Mineralogy, University of Padova*, 30, 1-31.
- Reiners P.W., Carlson R.W., Renne P.R., Cooper K.M., Granger D.E., McLean N.M., & Schoene B. (2018), *Geochronology and thermochronology*. John Wiley & Sons. doi: 10.1002/9781118455876
- Rudnick, R.L., & Gao, S. (2014), Composition of the continental crust. In *Treatise on Geochemistry 2nd Edition*, 4, 1-51. doi: <https://doi.org/10.1016/B978-0-08-095975-7.00301-6>
- Santamaría-López, A., Lanari, P., & Sanz de Galdeano, C. (2019), Deciphering the tectono-metamorphic evolution of the Nevada-Filábride complex (Betic Cordillera, Spain) – A petrochronological study. *Tectonophysics*, 767. doi: 10.1016/j.tecto.2019.06.028
- Schardt, H. (1903), Le profil géologique et la tectonique du massif du Simplon. *Eclogae Geologicae Helvetiae*, 8, 173-200.
- Soom, M.A. (1990), *Abkühlungs- und Hebungsgeschichte der Externmassive und der penninischen Decken beidseits der Simplon-Rhone-Linies seit dem Oligozän: Spaltspurdatierungen an Apatit/Zirkon und K-Ar-Datierungen an Biotit/Muskowit (westliche Zentralpen)*, (Doctoral dissertation). Bern: University of Bern.
- Steck, A. (2008), Tectonics of the Simplon massif and Lepontine gneiss dome: Deformation structures due to collision between the underthrusting European plate and the Adriatic indenter. *Swiss Journal of Geoscience*, 101, 515-546.
- Steck, A., & Hunziker, J. (1994), The Tertiary structural and thermal evolution of the Central Alps – compressional and extensional structures in an orogenic belt. *Tectonophysics*, 238, 229-254. doi: 10.1016/0040-1951(94)90058-2

- Steffen, K.J., & Selverstone, J. (2006), Retrieval of P-T information from shear zones: Thermobarometric consequences of changes in plagioclase deformation mechanisms. *Contributions to Mineralogy and Petrology*, 151, 600-614. doi: 10.1007/s00410-006-0073-8
- Stipp, M., Stünitz, H., Heilbronner, R., & Schmid, S. (2002), The eastern Tonale fault zone: A ‘natural laboratory’ for crystal plastic deformation of quartz over a temperature range from 250 to 700°C. *Journal of Structural Geology*, 24, 1861-1884. doi: 10.1016/S0191-8141(02)00035-4
- Stöckhert, B., Brick, M. R., Kleinschrodt, R., Hurford, A. J., & Wirth, R. (1999), Thermochronometry and microstructures of quartz – a comparison with experimental flow laws and predictions on the temperature of the brittle-plastic transition. *Journal of Structural Geology*, 21, 351-369. doi: 10.1016/S0191-8141(98)00114-X
- Stockli D.F. (2005), Application of low-temperature thermochronology to extensional tectonic settings. *Reviews in Mineralogy and Geochemistry*, 58, 411-448. doi: <https://doi.org/10.2138/rmg.2005.58.16>
- Studer, B. (1853), *Geologie der Schweiz*. Zurich: Stämpflische Verlagshandlung Bern and Friedrich Schulthess Zürich.
- Tectonic Map of Switzerland (1:500'000, GK500)*. (2005), Bern, Switzerland: Institute of Geology, University of Bern and Federal office for Water and Geology. Retrieved from Swisstopo (<https://www.swisstopo.admin.ch/>). ISBN 3-906723-56-9
- Thomas J.B., Watson E.B., Spear F.S., Shemella P.T., Nayak S.K., & Lanzirotti A. (2010), TitaniQ under pressure: the effect of pressure and temperature on the solubility of Ti in quartz. *Contributions to Mineralogy and Petrology*, 160, 743-759. doi 10.1007/s00410-010-0505-3
- Thomas, J.B., Watson, E.B., Spear, F.S., & Wark, D.A. (2015), TitaniQ recrystallized: Experimental confirmation of the original Ti-in-quartz calibrations. *Contributions to Mineralogy and Petrology*, 169. doi: 10.1007/s00410-015-1120-0
- Vance, D., & O’Nions, R.K. (1992), Prograde and retrograde thermal histories from the central Swiss Alps. *Earth and Planetary Science Letters*, 114, 113-129. doi: 10.1016/0012-821X(92)90155-O
- Wagner, G.A., Reimer, G.M., & Jäger, E. (1977), Cooling ages derived by apatite fission-track, mica Rb-Sr and K-Ar dating: The uplift and cooling history of the central Alps. *Memoirs of the Institute of Geology and Mineralogy, University of Padova*, 30, 1-27.
- Waldbaum, D.R., & Thompson, J.B. (1968), Mixing properties of sanidine crystalline solutions: II. Calculations based on volume data. *American Mineralogist*, 53, 2000-2017.
- Wark D.A., & Watson E.B. (2006), TitaniQ: a titanium-in-quartz geothermometer. *Contributions to Mineralogy and Petrology*, 152, 743-754. doi 10.1007/s00410-006-0132-1
- Wedepohl, K.H. (1995), The composition of the continental crust. *Geochimica et Cosmochimica Acta*, 59, 1217-1232. doi: [doi.org/10.1016/0016-7037\(95\)00038-2](https://doi.org/10.1016/0016-7037(95)00038-2)

- 1088 White, R.W., Powell, R., Holland, T.J.B., Johnson, T.E., & Green, E.C.R. (2014), New mineral
1089 activity-composition relations for thermodynamic calculations in metapelitic systems. *Journal of*
1090 *Metamorphic Geology*, 32, 261-286. doi: 10.1111/jmg.12071
- 1091 Zuza, A.V., & Cao, W. (2020), Seismogenic thickness of California: Implications for thermal
1092 structure and seismic hazard. *Tectonophysics*, 228426, 1-13. doi: 10.1016/j.tecto.2020.228426
- 1093 Zwingmann, H., & Mancktelow, N. (2004), Timing of Alpine fault gouges. *Earth and Planetary*
1094 *Science Letters*, 223, 415-425. doi: 10.1016/j.epsl.2004.04.041